PHYSICAL REVIEW A VOLUME 47, NUMBER 1 JANUARY 1993

Atoms in strong crossed electric and magnetic fields: Evidence for states with large electric-dipole moments

G. Raithel, M. Fauth, and H. Walther
Max-Planck-Institut für Quantenoptik and Sektion Physik der Universität München, D-8046 Garching, Federal Republic of Germany

(Received 16 September 1991; revised manuscript received 4 May 1992)

This paper reports on the evidence for large permanent electric-dipole moments of Rydberg atoms in crossed electric and magnetic fields. It was found that the dipole moments have a large value if the scaled electric-field strength $\epsilon = E\,B^{-4/3}$ has the value $\epsilon \approx 0.75$ (with electric- and magnetic-field strengths E and B in atomic units). The experimental technique employed to determine the atomic dipole moment was to add a slight inhomogeneity to the electric field and to measure the deflection of the atoms, this deflection being proportional to the field inhomogeneity and the atomic dipole moment. In order to discuss the experimental results, different theoretical approaches to the $\mathbf{E}\times\mathbf{B}$ problem are reviewed. The occurrence of Rydberg atoms with large dipole moments can be explained as being caused by a distinct type of classical orbit.

PACS number(s): 32.60.+i, 32.30.Jc, 35.10.Di

I. INTRODUCTION

Rydberg atoms in external microwave and static fields as well in magnetic or electric fields, or in combinations of the two, have been of great interest recently since the classical treatment of those systems shows chaotic behavior in certain field regions; it is therefore interesting to look for indicators of this chaotic behavior in the observed spectra. In the present article we would like to concentrate on atoms in strong external crossed electric and magnetic fields. Crossed fields occur rather frequently, for example, in a plasma confined by a magnetic field or on the surface of neutron stars. Rydberg atoms are suited for laboratory experiments, since the experimentally achievable field strengths are comparable to the inneratomic field acting on the Rydberg electron, and therefore the strong-field regime can be achieved easily. Moreover, due to the correspondence principle, semiclassical approximations are justified for Rydberg atoms. Due to the lack of quantum-mechanical calculations on Rydberg atoms in strong crossed fields at high excitation energies, such a simplified treatment is the only way to interpret our experimental results.

Rydberg atoms in weak magnetic and weak crossed electric and magnetic fields were investigated theoretically by Solov'ev [1–3] and Braun [3, 4] using perturbation theory. Based on this work Liberman, Pinard, and co-workers explained the low-field spectra of lithium in weak magnetic fields and weak parallel electric and magnetic fields [5–10]. Gay and co-workers [11, 12] and Korevaar and Littman [13] investigated alkali-metal Rydberg atoms in weak crossed fields theoretically as well as experimentally.

Classical chaos is observed in higher external fields when the influence of the external fields becomes comparable to that of the internal Coulomb field; this is the regime which is of particular interest for the present work. In experiments with Rydberg atoms in the classically chaotic regime it was found that the excitation spectrum shows sinusoidal modulations of the spectral intensity. The most pronounced modulations in the so-called quasi-Landau (QL) region were first discovered by Garton and Tomkins in 1969 [14]. The maxima observed are separated by about $1.5\hbar\omega_c$ (ω_c is the cyclotron frequency). Above the ionization limit the separation approaches $\hbar\omega_c$. These resonances were explained by Edmonds and Starace using a WKB approximation [15, 16]. Later highly excited alkali-metal atoms were investigated in external magnetic fields using high-resolution laser techniques. Approaching the zero-field ionization limit, strong lines appear which were interpreted by Kleppner and co-workers as QL resonances which were found to emerge from single quantum-mechanical states [17]. For higher excitation energies and higher magnetic fields these resonances are broadened and appear as sinusoidal modulations, the maxima of which follow WKB quantization in the plane perpendicular to the magnetic field [18, 19]; they were in agreement with the original QL spectra of Garton and Tomkins. It should be mentioned that there are also measurements performed on lithium Rydberg atoms in strong magnetic fields which exhibit QL resonances (for a review see Ref. [10]).

Further systematic experimental studies of QL spectra of hydrogen in strong magnetic fields were carried out by Welge and co-workers. They identified many new resonances in the Fourier transform of the spectra in addition to the one showing a spacing $1.5\hbar\omega_c$ [20–22]. It was possible to interpret these as arising from classical trajectories. In addition to the orbit which generates the QL resonances observed by Garton and Tomkins, and which only spreads out in the plane perpendicular to the magnetic field, other orbits extending in the magnetic-field direction were also observed. Recently Kleppner and co-workers investigated high-resolution lithium spectra in strong magnetic fields in an energy region above the ionization limit [23]. The spectra were explained very well by Gay and Delande using the complex-rotation method [24].

The influence of classical trajectories on oscillator strength, level density, and wave functions was investigated theoretically by Gutzwiller [25–29], Berry [30], Reinhardt [31], Wintgen, Friedrich, and Hoenig [32–35], Wunner and co-workers [36], Heller [37], and Bogomolny [38]. A semiclassical theory developed by Du and Delos describing the average oscillator strength allows a quantitative comparison between experimentally obtained Fourier spectra and properties of classical trajectories [39, 40]. The theoretical results important for this paper are summarized in Sec. III. In crossed electric and magnetic fields an interesting class of electron trajectories spinning around the classical ionization saddle point was found [41]. In principle recurring trajectories which contain an arbitrary number of cycles around the classical ionization saddle point exist as well [42]; however, due to the lack of stability the existence of detectable QL resonances associated with those orbits is quite unlikely.

The question which we want to address is whether classical trajectories not only lead to QL resonances in the spectra of highly excited Rydberg atoms in strong fields, but also allow interpretation of other properties of the atoms which can be determined experimentally. In this paper we directly measure a very fundamental property: the permanent electric-dipole moment. As shown in an earlier paper [42] the excitation spectra of rubidium in crossed fields can be decomposed into well-defined intensity modulations associated with classical trajectories. In Sec. IV the Fourier transforms of a few of those spectra are presented, and the Fourier components are related to classical trajectories. Since in Sec. II the importance of the paramagnetic term is discussed it should be mentioned for the sake of clarity that *all trajectory calculations* in this paper include the paramagnetic term, i.e., the results derived from these calculations are gauge independent. The properties of trajectories which display a large dipole moment are discussed in more detail, as individual wave functions may be scarred [35] by these trajectories and may thus lead to large dipole deflections observed in the experiment. The discussion of these orbits is the basis of our interpretation of the presented experimental results.

Section II reviews the theory of the hydrogen atom in crossed fields. When describing highly excited and in particular ionized atoms in crossed fields it is possible to obtain a Hamiltonian for the relative motion via a pseudoseparation. This Hamiltonian gives rise to wave functions localized in a two-dimensional-oscillator minimum displaced from the Coulomb center. The oscillator potential reproduces the fact known from classical electrodynamics that two $\mathbf{E} \times \mathbf{B}$–drifting particles keep a fixed average distance when the motion is averaged over a time larger than the cyclotron period of the heavier particle. However, the experiments presented here are performed below the ionization energy. In the infinite-mass approximation of the proton the Hamiltonian of hydrogen in strong crossed electric and magnetic fields consists of the kinetic energy, the paramagnetic term, and three terms describing different potentials: the Coulomb potential, the electric potential, and the diamagnetic potential. Since the diamagnetic term scales like B^2, whereas the paramagnetic term simply depends on B, one is tempted to omit the paramagnetic term, thus reducing the Hamiltonian to the dynamics of a particle in the sum potential. In the symmetric gauge this sum potential exhibits a feature which in recent years was discussed in several papers, for example, in Refs. [43–45]: For any value of the magnetic field there exists an electric-field strength, which, when exceeded, causes an outer minimum in the sum potential. Contrary to the oscillator potential mentioned above this outer potential minimum is a gauge-dependent artifact which is clearly unphysical. However, there is numerical evidence that *below* the ionization energy the potential in the symmetric gauge gives a reasonable estimate of the space region which is covered by classical trajectories launched at the Coulomb center. This feature is discussed in Sec. II B.

Experimentally it has already been demonstrated that in crossed fields Rydberg atoms with large electric-dipole moments exist [45]. In this paper improved experiments are presented, which are performed with a more sophisticated experimental setup than the one described in Ref. [42]. Using the electric-dipole deflection in an electric field with a well-defined field inhomogeneity the electric-dipole moments of the atoms in crossed fields could be studied.

The possibility of measuring dipole deflections requires some special features in the experimental setup. The beam of rubidium atoms, which must be parallel to the magnetic-field lines, needs to be velocity selected. The electric field must have an adjustable inhomogeneity, and the electric and magnetic fields have to be well defined not only at the excitation point, but also along the entire deflection region. Furthermore, the field ionization and the detection of the ejected electrons must be position sensitive, therefore it is necessary to ensure that the drift motion of the electrons ejected in the field ionization region does not influence the observed deflection pattern in an uncontrollable way. Since the number of deflected atoms is relatively small, it is necessary to be certain that no spurious signals are produced by uv-generated photoelectrons or by electrons originating from Rydberg atoms ionized before they reach the field ionization zone. In Sec. V the experimental setup which fulfills these requirements is described.

Since the relative number of strongly deflected atoms is very small it is necessary to confirm the results by different experiments, thus excluding systematic errors. In Sec. VI results obtained in two different types of dipole-deflection experiments are shown. The first method was to integrate the atomic-beam image for a long time, keeping the laser excitation energy and the field values fixed. This type of experiment minimizes the statistical fluctuations originating in the dark counts of the detection system. A second technique was to sample the dipole-deflection signals at fixed field values as a function of the excitation energy. The statistical fluctuations in this type of experiment are larger, but the deflection patterns agree with the first type of experiment and thus increase the confidence in the results.

The experimentally found Rydberg atoms exhibiting large dipole moments are interpreted in Sec. VI quantitatively utilizing classical orbits as discussed in Sec. IV. The semiclassical explanation of the dipole-deflection experiments represents our current interpretation of the experimental results. There is the hope that increasing computer capabilities will allow one to perform exact quantum calculations so that a better and more accurate comparison between theory and experiment will be possible.

II. ONE-ELECTRON SYSTEMS IN STRONG CROSSED FIELDS: THEORETICAL ASPECTS

The systems of interest in this paper are hydrogenlike Rydberg atoms in strong crossed electric and magnetic fields (rubidium in our case). The electric field alone lowers the ionization energy W_{ion} of the atoms by an amount following fairly well the value derived classically [46]:

$$W_{\text{ion}} = -2\sqrt{E} \tag{1}$$

with W_{ion} and the electric-field strength E in atomic units. We find experimentally that an additional magnetic field increases the ionization energy by only a few wave numbers. Classical trajectory calculations in crossed fields as well as quantum calculations in the pure electric-field case suggest that crossed fields support states with large dipole moments only in the energy range near the classical ionization energy Eq. (1). Therefore Eq. (1) in connection with the zero-field ionization energy of the $5S_{1/2}$ ground state approximately yields the laser frequency which has to be used in the experiment, as a function of the electric-field strength E. The magnetic-field-free quasienergy levels can be calculated numerically employing the fact that the combined non-Coulombic alkali and electric potential deviates from the corresponding separable hydrogenic case only within the core region [47]. Due to the high level density in the vicinity of the ionization threshold, even a small additional magnetic field brings the system into a regime where the cyclotron frequency ω_c exceeds the level spacings without magnetic field. This regime is called the "strong-field-mixing regime" in the electric field-free case (see Ref. [48] and references therein). Since in our experiments the influence of the Coulomb force, the electric field, and the magnetic field on the Rydberg electron are of the same order of magnitude, perturbation theory based on the field-free eigenstates is not adequate and a treatment starting from a more fundamental level is necessary.

In the theoretical description of the system a major question is whether it is accurate to assume an infinite mass of the positive particle. This infinite-mass approximation cannot be applied when dealing with states in the $\mathbf{E} \times \mathbf{B}$—continuum, which can be considered as ionized atoms in crossed fields. This regime is discussed in Sec. II A. In our experiments we deal with highly excited Rydberg atoms below the ionization limit. In this case, which is discussed in Sec. II B, the infinite-mass approximation is reasonable.

A. Ionized atoms in crossed fields

Many authors emphasize that due to the nonconservation of the total canonical momentum of two interacting particles in a magnetic field as well as in crossed fields a complete theoretical description of such systems must originate in the genuine two-body Hamiltonian [49–51] which is written according to the principle of minimal coupling as i

$$H = \frac{1}{2m_e}[\mathbf{p}_e + e\mathbf{A}(\mathbf{r}_e)]^2 + \frac{1}{2m_p}[\mathbf{p}_p - e\mathbf{A}(\mathbf{r}_p)]^2 + e\mathbf{E}\cdot(\mathbf{r}_e - \mathbf{r}_p) - \frac{e^2}{4\pi\epsilon_0|\mathbf{r}_e - \mathbf{r}_p|} \tag{2}$$

with vector potential $\mathbf{A}$, electric field $\mathbf{E}$, and subscripts e and p referring to the electron and the positive nucleus, respectively.

The invariance of this Hamiltonian with respect to translations is generated by a generalized momentum operator which contains not only the sum of the individual canonical momenta, but also a term performing a gauge transformation which shifts the vector potential according to the desired particle translation. Choosing the symmetric gauge, the generalized momentum takes the form

$$\mathbf{P}_p = \mathbf{P} - \frac{e}{2}\mathbf{B} \times \mathbf{r}, \tag{3}$$

where $\mathbf{P}$ is the total canonical momentum, which in the quantum-mechanical description is $\frac{\hbar}{\mathrm{i}}\frac{\partial}{\partial \mathbf{R}}$ with center-of-mass (c.m.) coordinate $\mathbf{R}$, and $\mathbf{r} = \mathbf{r}_e - \mathbf{r}_p$.

In neutral systems like the one considered in this paper the components of the generalized momentum commute with H [Eq. (2)] as well as with each other. The eigenfunctions of H [Eq. (2)] can be chosen in the form

$$\psi(\mathbf{R}, \mathbf{r}) = \psi_{\text{rel}}(\mathbf{r})\mathrm{e}^{\mathrm{i}(\mathbf{P}_p + \frac{e}{2}\mathbf{B}\times\mathbf{r})\cdot\mathbf{R}/\hbar} , \tag{4}$$

which are eigenfunctions with eigenvalue $\mathbf{P}_p$ of operator $\hat{\mathbf{P}}_p$ [Eq. (3)]. Inserting Eq. (4) in the Schrödinger equation with H [Eq. (2)] yields the Hamiltonian governing the relative motion (RM) [49]:

$$H_{\text{rel}} = \frac{p^2}{2\mu} + \frac{e\delta}{2\mu}\mathbf{B}\cdot(\mathbf{r} \times \mathbf{p})\frac{e^2}{8\mu}(\mathbf{B} \times \mathbf{r})^2 + \frac{e}{M}(\mathbf{P}_p \times \mathbf{B})\cdot\mathbf{r} + e\mathbf{E}\cdot\mathbf{r} - \frac{e^2}{4\pi\epsilon_0 r} + \frac{P_p^2}{2M} , \tag{5}$$

where $M = m_e + m_p$, $\mu = \frac{m_e m_p}{M}$, $\delta = \frac{m_p - m_e}{M}$.

Since the c.m. motion enters the equation of the RM via the coupling term $\frac{e}{M}(\mathbf{P}_p \times \mathbf{B})\cdot\mathbf{r}$, which contains $\mathbf{P}_p$, Eq. (5) is not really separated from the c.m. motion but is coupled to it by a conserved quantity. This is called a pseudoseparation.

The Hamiltonian in Eq. (5) displays two interesting differences with respect to the Hamiltonian which is obtained by just adding electric- and magnetic-field terms to the undisturbed RM Hamilton operator of hydrogen:

(i) The g factor of the angular momentum deviates from the value 1 by the factor $g = \delta = \frac{m_p - m_e}{M}$, this being a very small deviation due to the large nuclear mass. This correction was also found in Ref. [52] for the pure magnetic-field case.

(ii) The generalized momentum is connected to the c.m. velocity and the relative coordinate $\mathbf{r}$ by $\mathbf{P}_p = M\mathbf{V} - e(\mathbf{B}\times\mathbf{r})$. Therefore the contribution $\frac{e}{M}(\mathbf{P}_p\times\mathbf{B})\cdot\mathbf{r}$ in Eq. (5) which looks like a potential in a constant electric field $\frac{1}{M}(\mathbf{P}_p \times \mathbf{B})$ is essentially composed of a motional electric field $\mathbf{V} \times \mathbf{B}$ and an additional "virtual" field $-\frac{e}{M}(\mathbf{B} \times \mathbf{r}) \times \mathbf{B}$. Since only the sum of the external electric field and the $\mathbf{P}_p$-induced field enters the RM equation, many different systems having just the same net electric field $\mathbf{E}_{\text{net}} = \mathbf{E}_{\text{external}} + \frac{e}{M}(\mathbf{P}_p\times\mathbf{B})$ exhibit the same RM dynamics. A net electric-field value in Eq. (5) may result exclusively from an actual applied external field, from a large c.m. velocity $\mathbf{V}$ perpendicular to $\mathbf{B}$, or also from a large relative coordinate $\mathbf{r}$ which can be chosen arbitrarily via the initial conditions (at least in theory). For example, all net (crossed) electric-field values $\mathbf{E}_{\text{net}}$ can be realized without applying any external electric field by taking particles at rest, i.e., $\langle\mathbf{v}_i\rangle = 0$, and bringing the centers of their wave functions $\langle\mathbf{r}_i\rangle$ to two locations differing by $\mathbf{r} = -\frac{Me^2}{B^2}\mathbf{E}_{\text{net}}$.

Inserting the transformation

$$\psi(\mathbf{r}) = \phi(\mathbf{r}_r - \mathbf{r}_0)e^{i\delta\mathbf{r}_r\cdot\mathbf{P}'_p/2\hbar}$$

into the Schrödinger equation with H_{rel} [Eq. (5)] yields another Hamiltonian for the transformed wave function ϕ [49]:

$$\tilde{H}_{\text{rel}} = \frac{p_r^2}{2\mu} + \frac{e\delta}{2\mu}\mathbf{B}\cdot(\mathbf{r}_r \times \mathbf{p}_r) + \frac{e^2}{8\mu}(\mathbf{B}\times\mathbf{r}_r)^2 - \frac{e^2}{4\pi\epsilon_0|\mathbf{r}_r + \mathbf{r}_0|} + \frac{P_p^2}{2M} - \frac{P_p'^2}{2M}\,, \tag{6}$$

with $\mathbf{P}'_p = \mathbf{P}_p + \frac{M}{B^2}\mathbf{B}\times\mathbf{E}$ and $\mathbf{r}_0 = \frac{1}{eB^2}\mathbf{B}\times\mathbf{P}'_p$.

This is the Hamiltonian of a two-dimensional harmonic oscillator with an additional paramagnetic term and a Coulomb perturbation sitting on the side of the oscillator potential.

If one considers the classical system, two $\mathbf{E}\times\mathbf{B}$–drifting particles, the physical interpretation of the oscillator potential in Eq. (6) becomes clear: Due to the particle-independent drift velocity $\frac{E}{B}$ the oscillator potential describes the oscillation of the RM coordinate between two noninteracting $\mathbf{E}\times\mathbf{B}$–drifting particles about their average separation [equal to $\mathbf{r}_0$ in Eq. (6)]. Thus, wave functions located in the oscillator minimum plotted in Fig. 1 correspond to an $\mathbf{E}\times\mathbf{B}$–drifting two-particle system with negligible Coulomb interaction between the particles.

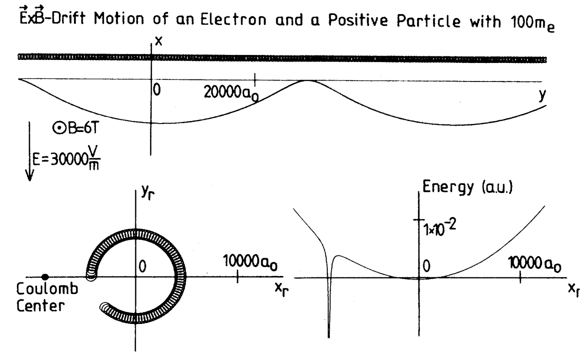

FIG. 1. Unperturbed $\mathbf{E} \times \mathbf{B}$–drift motion of an electron and a positive particle with mass $100m_e$, both particles having no energy in the z direction (upper part of the figure). The mass of the positive particle was chosen as $100m_e$ so that the cyclotron motion could be displayed on the figure. The relative motion in (x_r, y_r) is localized in space, thus it can be described via the two-dimensional oscillator potential depicted at the bottom of the figure. The system is quasibound via the external fields, but it does not behave such as an atom: An inhomogeneous electric field separates the particles due to different drift velocities E/B. A truly bound system such as an atom, however, would be deflected as a whole. If the parameters would be chosen in such a way that the two particles would come close together, the Coulomb interaction would couple states with different l_z; the description of the dynamics by the potential alone would be no longer sufficient.

The oscillator potential results solely from the localizing effect of the external fields on both constituents of an ionized atom. The wave function associated with the shifted RM coordinate $\mathbf{r}_r$ may be localized in the oscillator minimum (see also Fig. 1). Now we ask the question when is it allowable to plot the sum potential as in Fig. 1? Clearly this is allowed if the paramagnetic term in Eq. (6) is conserved. This is the case for wave functions localized in the oscillator minimum of Fig. 1 which do not overlap with the Coulomb potential: for such unperturbed Landau states both the z component of angular momentum l_z and the paramagnetic term in Eq. (6) would be conserved. Thus, talking about low-lying wave functions in the potential plotted in Fig. 1 makes sense. However, if a wave function calculated in the potential plotted in Fig. 1 overlaps significantly the Coulomb potential, the cylindrical symmetry is broken and thus l_z is no longer conserved. With increasing temporal variation of l_z the wave functions deduced from the potential terms alone lose their physical significance. Thus, the answer to the above addressed question is in the parameter range where wave functions in the oscillator potential do not overlap with the Coulomb potential, the potential curve plotted in Fig. 1 is of physical significance. Adopting a gauge which is not as well adapted to the symmetry of the problem would change the situation: in the case of an asymmetric gauge the paramagnetic term would not be conserved in any parameter range. Neglecting the paramagnetic term and considering the dynamics in the remaining potential terms would be wrong. Thus, due to the cylindical symmetry of the non-Coulomb part of the Hamiltonian Eq. (6) the diamagnetic potential in the symmetric gauge is of physical significance (in a certain parameter range), diamagnetic potentials in an asymmetric gauge are useless if the corresponding paramagnetic term is neglected.

If the parameters are chosen such that a Landau-type wave function in the diamagnetic potential is only slightly perturbed by the Coulomb potential, the influence of the Coulomb interaction can be treated as a perturbation acting on the Landau states of the potential plotted in Fig. 1, as was done by Gor'kov and Dzjaloshinskii [49] for excitons in crossed fields.

B. Stable Rydberg atoms in crossed fields

As discussed, Eq. (6) is the natural way to describe by perturbation theory the dynamics of $\mathbf{E}\times\mathbf{B}$–drifting particles weakly interacting via a Coulomb potential. There is another limit: For atomic systems in the regime where the Coulomb force is still strong enough to bind the electron strongly to the positive ion, the wave functions are located in the outer minimum which in Fig. 1 is called the "Coulomb center." Due to the strong nonconservation of l_z in that case the oscillator potential plotted in Fig. 1 is unphysical. Though correct, the Hamiltonian $\tilde{H}_{\rm rel}$ [Eq. (6)] does not provide any advantage in this case, since with the conservation of l_z the reduction of the dynamics to a potential problem is lost as well. However, now it is possible to make the infinite-mass approximation for the positive ion. This can be concluded from the experiment: we are dealing with Rydberg atoms passing a crossed field region which does not change the c.m. motion. (The electric-dipole deflection which occurs if the electric field is slightly inhomogeneous is independent of the $\mathbf{E}\times\mathbf{B}$–drift motion discussed here.) No change of the c.m. momentum essentially means the *positive particle* does not change kinetic momentum, i.e., infinite mass of the positive particle can be assumed. In the infinite-mass approximation Eq. (6) makes no sense; thus it is necessary to use $H_{\rm rel}$ [Eq. (5)], which in the limit $m_p \rightarrow \infty$ yields the Hamiltonian commonly used when considering the hydrogen atom in external fields and which will be written in the following form for convenience, with $\mathbf{B} = B\mathbf{e}_z$ and $\mathbf{E} = -E\mathbf{e}_x$:

$$h = \frac{p^2}{2m_e} + \frac{e}{2m_e}Bl_z + \frac{e^2B^2}{8m_e}(x^2+y^2) - eEx - \frac{e^2}{4\pi\epsilon_0 r} \ . \tag{7}$$

This Hamiltonian accurately describes the stable Rydberg atoms observed in our experiments. However, when writing down this Hamiltonian one has to keep in mind that, as follows from the preceding section, the infinite-mass approximation for the positive ion completely loses its meaning as soon as the atom is ionized into the $\mathbf{E}\times\mathbf{B}$ continuum.

h [Eq. (7)] has no continuous symmetries, but there are two discrete symmetries which can be employed to find classical recurring or periodic trajectories of the system (see Sec. IV) and which allow one to draw conclusions concerning the dipole moments of stationary wave functions:

(i) P_z symmetry. For nondegenerate energy levels (in this system degeneracies are accidental) the wave functions have the property $\psi(x,y,-z) = \pm\psi(x,y,z)$; thus $\langle z\rangle = 0$ (no dipole moment in the z direction).

(ii) TP_y symmetry. The wave functions have the property $\psi(x,-y,z) = \pm\psi^*(x,y,z)$, and thus $\langle y\rangle = 0$. This coincides with the experimental observation that no states exist with an electric-dipole moment in the y direction: Since $\mathrm{div}\mathbf{E}(x,y) = 0$, a field inhomogeneity I in the x direction implies an inhomogeneity $-I$ in the y direction, acting on y components of dipole moments. However, as mentioned already, a deflection in the y direction has never been observed.

In analogy to Fig. 1 the potential terms in h [Eq. (7)] give a total potential

$$U(\mathbf{r}) = \frac{e^2B^2}{8m_e}(x^2+y^2) - eEx - \frac{e^2}{4\pi\epsilon_0 r} \tag{8}$$

which exhibits an outer potential minimum, if the electric field fulfills

$$E > B^{4/3}\left(\frac{27e^3}{256m_e^2\pi\epsilon_0}\right)^{1/3} , \tag{9}$$

i.e., the scaled electric-field strength $\epsilon = E\,B^{-4/3}$ is larger than 0.75 (with E and B in atomic units).

In contrast to Fig. 1 and Eq. (6), where for large E and $\mathbf{P}_p = \mathbf{0}$ the displacement between Coulomb and oscillator minimum $r_0 \approx \frac{ME}{eB^2}$ is proportional to the total mass, in the case of Eq. (8) it is now determined by the much smaller electron mass $r_0 \approx \frac{4m_eE}{eB^2}$.

The most exciting question about the potential in Eq. (8) is whether, as in the case of the oscillator minimum displayed in Fig. 1, the "small scale" oscillator minimum also leads to real electronic states. *The answer is no*: If one assumes an electron sitting in the outer minimum of the potential given by Eq. (8), not the Coulomb field but the external fields E and B would determine its motion, i.e., the electron would immediately be ionized into the $\mathbf{E}\times\mathbf{B}$–continuum. This ionization cannot be described by the potential Eq. (8) since the description of the $\mathbf{E}\times\mathbf{B}$–drift requires the paramagnetic term. Formally the situation is clear: The potential in Eq. (8) does not have cylindrical symmetry, thus l_z is not conserved and especially the outer potential minimum has no physical meaning at all. Thus the following considerations are strictly restricted to situations where the atom has not been ionized. If the electron has passed the classical ionization saddle point none of the statements found in the following paragraphs hold.

In the following the possibility of obtaining some physical information in the sum of electric and diamagnetic potential Eq. (8) will be discussed. The necessary condition for an approximately constant paramagnetic term in the symmetric gauge is that the potential should have cylindrical symmetry in the region where the wave function's amplitude is large. This symmetry is approximately fulfilled if at the considered electron energy (and thus wave-function extension) the magnetic field or the Coulomb field is strongly dominating. The case of dominating Coulomb field can be treated by perturbation theory. If the magnetic field dominates then the influence of the weak electric field can be treated by perturbation theory also. However, the first-order perturbation is zero, and for the second-order perturbation one needs in principle the wave functions of the pure magnetic-field problem for all l_z manifolds being not easily obtainable. As the importance of the electric field increases the paramagnetic term becomes more and more time dependent. Especially, for an electric-field strength close to the ionization limit (this was the usual situation in our experiments) the paramagnetic term is highly nonconserved.

It has been mentioned in the literature [41] that the potential in Eq. (8) is gauge dependent. In the electric field-free case the paramagnetic term is conserved by choosing the *symmetric* gauge, which allows the study of the system by considering a static potential without paramagnetism (see, for example, [46]). Unfortunately, for stable Rydberg atoms in crossed fields in the parameter range where all forces (Coulomb, external electric, magnetic) are comparable no gauge yields an approximately conserved paramagnetic term; thus it is not possible to study the system by simply considering a certain potential. However, if one is only interested in very rough information on the atomic dipole moments, one could try to choose the gauge which *minimizes* the time dependence of the paramagnetic term. The following equation shows the potentials U(r), the corresponding paramagnetic terms $U_{\rm pm}(\mathbf{r},\mathbf{p})$, and the classical time derivatives of the paramagnetic terms $\frac{dU_{\rm pm}(\mathbf{r},\mathbf{p})}{dt}$ for the symmetric gauge $\mathbf{A} = \frac{B}{2}(-y,x,0)$ [Eq. (10a)] and the asymmetric gauges $\mathbf{A} = B(-y,0,0)$ [Eq. (10b)] and $\mathbf{A} = B(0,x,0)$ [Eq. (10c)] in atomic units:

$$\begin{aligned} U(\mathbf{r}) &= -\frac{1}{r} - Ex + \frac{B^2}{8}(x^2+y^2), \\ U_{\rm pm}(\mathbf{r},\mathbf{p}) &= \frac{B}{2}(xp_y - yp_x), \\ \frac{d}{dt}U_{\rm pm}(\mathbf{r},\mathbf{p}) &= -\frac{B}{2}Ey, \qquad (10a) \\ U(\mathbf{r}) &= -\frac{1}{r} - Ex + \frac{B^2}{2}y^2, \quad U_{\rm pm}(\mathbf{r},\mathbf{p}) = -Byp_x, \\ \frac{d}{dt}U_{\rm pm}(\mathbf{r},\mathbf{p}) &= -B\left(Ey - p_xp_y + \frac{xy}{r^3}\right), \qquad (10b) \\ U(\mathbf{r}) &= -\frac{1}{r} - Ex + \frac{B^2}{2}x^2, \quad U_{\rm pm}(\mathbf{r},\mathbf{p}) = +Bxp_y, \\ \frac{d}{dt}U_{\rm pm}(\mathbf{r},\mathbf{p}) &= B\left(p_xp_y - \frac{xy}{r^3}\right). \qquad (10c) \end{aligned}$$

Due to the different gauges the canonical momenta $\mathbf{p}$ are different in the three equations. In quantum mechanics, according to Ehrenfest's theorem, the time derivative of the paramagnetic term $\hat{U}_{\rm pm}$ is given by

$$\frac{d}{dt}\langle\hat{U}_{\rm pm}\rangle = \frac{\rm i}{\hbar}\langle[H,\hat{U}_{\rm pm}]\rangle , \qquad (11)$$

which yields the same expressions as those given in Eqs. (10a)–(10c), but the bras and kets have to be added. Thus, in order to estimate the order of magnitude of the temporal changes of the paramagnetic term in different gauges, it is possible to calculate the time-dependent paramagnetic energy for some classical trajectories with initial conditions $\mathbf{r}_i$ and $\mathbf{p}_i$ which are known to influence the system [42]. Here we have in mind that a wave packet with initial conditions $\langle\mathbf{r}\rangle = \mathbf{r}_i$ and $\langle\mathbf{p}\rangle = \mathbf{p}_i$ fol-

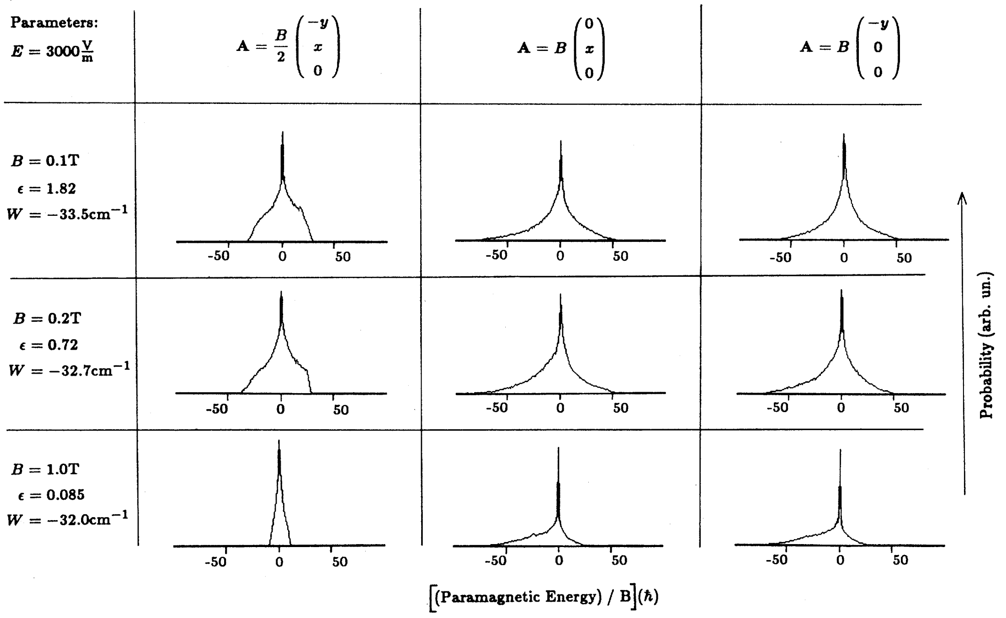

FIG. 2. Variations of the paramagnetic term in the data sets explained in the text. For the indicated parameters the probability distributions of finding a certain paramagnetic energy (divided by the magnetic field B) are plotted for three different gauges and three values of the scaled electric field vs that quantity. The excitation energy which has been used in the trajectory calculations was just below the experimentally observed ionization limit. The figure shows that the variations of the paramagnetic energy are minimized by adopting the symmetric gauge, even for quite large scaled electric field.

lows more or less the classical trajectory within a certain time. This was done for some of the trajectories shown in Fig. 5. As expected, in all three gauges the paramagnetic term changed strongly, whereby the changes in the symmetric gauge were smallest. Especially for orbits which do not extend too far in the y direction the changes of the paramagnetic term are moderate, as can be seen from Eq. (10a), which for $y = 0$ yields a constant paramagnetic term. In the limit $E \longrightarrow 0$ only the symmetric gauge allows one to neglect the paramagnetic term [see Eqs. (10a)–(10c)].

In Fig. 2 the results of a more general numerical test are shown. Classical electrons were launched radially from the Coulomb center in directions covering the whole 4π sphere. The fields and the energy have been chosen to match the experimentally observed ionization threshold. The trajectories were integrated for about 15 cyclotron periods. The electron position and momentum were recorded about ten times per cyclotron period. Additionally each point where the trajectory passed a maximum distance from the core was recorded. On evaluation of the data the paramagnetic energy was calculated using Eqs. (10a)–(10c). Since trajectories starting in many directions were integrated for a quite long time the obtained spread is a measure of how well the different gauges conserve the paramagetic energy (which in the investigated gauges initially is zero for trajectories starting radially at the center). The described procedure was performed for different values of the scaled electric field $\epsilon = EB^{-4/3}$. Figure 2 shows the obtained probability distributions of the paramagnetic energy in atomic units, divided by B. Obviously the variation of the paramagnetic term is minimized by the symmetric gauge, even in the case of quite strong electric fields. Again it must be emphasized that this holds *only if the atom is not ionized.* As the electron goes beyond the classical ionization saddle point the paramagetic energy spreads out dramatically.

Since in the experiment electric-dipole moments were measured, it is quite interesting to check whether it is possible to get estimates on the fraction of the configuration space which is actually covered by trajectories starting from the core. We were surprised to find that even for quite large electric fields the equipotential surface of the potential Eq. (8), taken at the actual excitation energy, quite accurately coincides with the surface which limits the configuration space region which is accessed by trajectories starting at the core. It is also interesting that the potential surfaces obtained by the asymmetric gauges give extremely bad estimates of the actually accessed space region. Again it should be noted that this observation is not valid for ionized atoms; one only finds this behavior if the energy is chosen below the experimentally observed ionization energy. Especially the outer potential minimum in the potential Eq. (8) is clearly unphysical and requires no further discussion. The mentioned numerical calculation was restricted to the space inside the classical ionization saddle point where the potential Eq. (8) has no fixed point. The results are displayed in Fig. 3. The data were the same as those also used for Fig. 2. The displayed projections of x and y

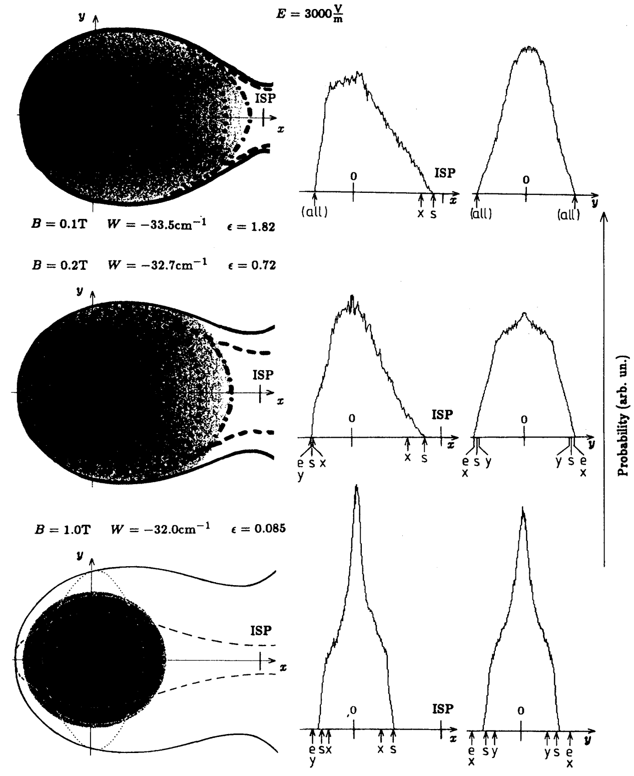

FIG. 3. Projection of the data which are evaluated in Fig. 2 onto the space coordinates x,y (z is not interesting since the diamagnetic potential has no z component). On the left-hand side of the figure the projections of the data points onto the (x,y) plane are shown. The curves correspond to equipotential lines of the electric potential (solid), and of the electric potential plus the diamagnetic potential in the symmetric gauge (dash dotted), the gauge $\mathbf{A} = -By\,\mathbf{e}_x$ (dashed), or the gauge $\mathbf{A} = Bx\,\mathbf{e}_y$ (dotted). The energies of the equipotential lines are equal to the specified excitation energies. For clarity in the planar projection at $B = 1.0$ T no lines have been drawn inside the accessed space region. However, by continuation of the curves plotted outside that region it is easy to identify to which gauge the open lines inside the covered region correspond. The open line which has no continuation outside corresponds to the symmetric gauge. The spatial scale factor is determined by the indicated position of the classical ionization saddle point (ISP). On the right-hand side of the figure the probability of finding a data point with a certain value x (y) is plotted vs x (y). The scale factor again is determined by the indicated position of the ISP. The different arrows pointing at certain locations on the scales indicate the positions of equipotential lines associated with the following potentials: arrows labeled with e refer to the electric potential, and those labeled with s, x, y refer to the sum of electric potential and diamagnetic potential in the symmetric gauge (s), the gauge $\mathbf{A} = Bx\,\mathbf{e}_y$ (x) or the the gauge $\mathbf{A} = -By\,\mathbf{e}_x$ (y). The terminus (*all*) simply means that the equipotential lines cannot be resolved. It can be recognized that especially in the x direction the sum of the electric potential and the diamagnetic potential in the symmetric gauge describes the extension of the accessed configuration space best. For $\epsilon \rightarrow 0$ this statement is trivial, however, there is also quite good agreement in the case of high scaled electric-field ϵ.

values which are plotted in Fig. 3 show that the sum potential in the symmetric gauge gives the best estimate of the configuration space region which is covered by trajectories starting at the center. One also can recognize an asymmetry in the x distribution which increases with increasing scaled electric field ϵ.

In summary, the aim of these considerations was not to show that the potential obtained in the symmetric gauge describes the system well. It is clear that no potential model does so. Quantitative classical as well as quantum-mechanical calculations based on Eq. (7) require one to include the paramagnetic term. Especially the two fixed points of the potential Eq. (8) occurring when Eq. (9) is fulfilled are in a space region where Eq. (8) is meaningless anyway. We found that below the ionization energy in a space region with radii $|\mathbf{r}|$ well below those of the mentioned fixed points the symmetric gauge results in the smallest variations of the paramagnetic term. We also found that below the ionization energy the potential Eq. (8) gives a fairly good estimate of the configuration space volume which is accessed by classical trajectories starting at the center. Therefore the potential Eq. (8) may allow one to estimate the dipole moments of excited states better than the corresponding potentials obtained with asymmetric gauges.

It should be mentioned that a similar system exists in which the question about whether it is justified to neglect the paramagnetic term or not does not arise: electron layers on helium surfaces. In this system the force between the electron and its image plays the role of the Coulomb force, the electric field is directed into the helium bulk, and the magnetic field lies in the surface plane. This system has two simplifications with respect to a free atom: (i) it is a one particle system, and (ii) the "Coulomb force" depends only on the coordinate perpendicular to the surface.

As shown in Ref. [43] these differences allow one to choose an asymmetric gauge in order to reduce the problem to one dimension without making any approximation. The resulting one-dimensional Hamiltonian with effective image charge Qe is [43]

$$h_{\mathrm{liq\,He}} = \frac{p_x^2}{2m_e} + \frac{e^2B^2}{2m_e}x^2 - eEx - \frac{Qe^2}{4\pi\epsilon_0|x|} \ . \qquad (12)$$

Except for a factor of 4 which occurs in the diamagnetic term, the potential occurring in Eq. (12) is equal to that in Eq. (8) with $y = z = 0$. Rau *et al.* calculated by a WKB method energies of electron states trapped in this exotic type of surface potential. However, due to the fundamental differences discussed above, those results cannot be expected to show any agreement with atomic systems.

III. INFLUENCE OF CLASSICAL ORBITS ON SPECTRA AND WAVE FUNCTIONS

In recent years it was shown experimentally as well as theoretically that classical closed orbits influence quantum-mechanical properties, especially of highly excited systems which are supposed to approach the classical behavior. Gutzwiller derived a semiclassical approximation of the average level density which displays a feature common to semiclassical approximations of quantum-mechanical properties: the semiclassical formulas exhibit modulations which are related to classical closed orbits (Refs. [25–29] and references therein).

In the experiments described in this paper, not the level density but the oscillator strength between ground-state and Rydberg levels is measured. The oscillator strength exhibits modulations as well. The most prominent example are the quasi-Landau resonances discovered by Garton and Tomkins [14] in the photoabsorption spectra of Rydberg atoms in strong magnetic fields. Other types of QL resonances were found by Welge and co-workers in more sophisticated experiments [20–22]. As derived by Du and Delos these modulations can be explained quantitatively using the ground-state quantum numbers, the polarization of the exciting radiation, and purely classical properties of trajectories starting at the Coulomb center and returning to it. As shown in Refs. [39, 40] the energy-averaged oscillator strength in the vicinity of the field-free ionization limit can be approximated by

$$f(W) = f_0(W) + \sum_{\mathrm{cl}} C_{\mathrm{cl}} \sin(T_{\mathrm{cl}}W + \Delta_{\mathrm{cl}}) \ , \qquad (13)$$

where $f_0(W)$ is the field-free energy-averaged oscillator strength. The sum is taken over all recurring trajectories, where "recurring" does not mean periodic but only starting and terminating at the nucleus. T_{cl} is the time of traversal and Δ_{cl} is a trajectory-dependent phase. The data on laser polarization, ground state, and stability of the trajectories are contained in the modulation amplitudes C_{cl}, calculated in Refs. [39, 40]. Equation (13) shows that the Fourier transforms of ordinary spectra recorded as a function of the excitation energy at constant field values yield the times of traversal of the classical trajectories influencing the spectra.

As explained in Ref. [42], not ordinary spectra but recordings of scaled excitation spectra as a function of $B^{-1/3}$ are best suited for the identification of QL modulations in crossed fields. Scaled spectra require one to change the externally applied electric- and magnetic-field strengths E and B as a function of the energy of the excited Rydberg atoms W in order to keep the scaled parameters $\epsilon = EB^{-4/3}$ and $\omega = WB^{-2/3}$ constant. It is possible to write Eq. (13) in a form which facilitates comparison with experimental scaled excitation spectra:

$$f(B^{-1/3}) = f_0(B^{-1/3}) + B^{1/6} \sum_{\mathrm{cl}} C_{\mathrm{s,cl}} \sin(B^{-1/3} S_{\mathrm{s,cl}}) \ . \qquad (14)$$

$C_{\mathrm{s,cl}}$ are complex, scaled modulation amplitudes, which also contain the Maslov indices. The $C_{\mathrm{s,cl}}$ remain constant during the whole scaled scan as do the scaled action values $S_{\mathrm{s,cl}}$ of the trajectories. The modulation strength depends weakly on B via the factor $B^{1/6}$ in Eq. (14). As can be recognized from the argument of the sin in Eq. (14), the Fourier transforms of long scaled spectra yield accurate values of the scaled actions $S_{\mathrm{s,cl}}$ of the modulating trajectories.

The question of how the modulations of the oscillator strength are related to the electric-dipole moments of the atoms arises. The answer is given by Bogomolny, who shows in Ref. [38] that for systems exhibiting unstable periodic orbits and fulfilling semiclassical conditions anywhere in configuration space, the slightly space- and energy-averaged quantum-mechanical probability distributions can be semiclassically approximated by a mean part plus contributions resulting from periodic orbits:

$$\langle|\psi(q)|^2\rangle = \rho_0(q) + \hbar^{\frac{n-1}{2}} \times \sum_{\mathrm{PO}} \mathrm{Im}\langle A_{\mathrm{PO}}(x)\; e^{\frac{i}{\hbar}[S_{\mathrm{PO}} + W_{\mathrm{PO}}^{km}(x)\frac{y_k y_m}{2}]}\rangle \;. \tag{15}$$

Here n is the dimensionality of the system, and x and y_i are related to coordinate systems where the x axis is taken along the periodic orbits and the y_i in the transverse direction(s). The $\langle\,\rangle$ denotes the averaging process in space and on the energy scale. The mean part $\rho_0(q)$ is the projection of the classical microcanonical distribution onto the configuration space.

Equation (15) shows that the average probability distribution is enhanced in the neighborhood of classical periodic orbits. The strength of this enhancement depends on the stability of the orbits via $A_{\mathrm{PO}}(x)$ and $W_{\mathrm{PO}}^{km}(x)$ in Eq. (15) which follow from the classical stability of the periodic orbits. In agreement with Eq. (13) it was found experimentally [42] that atoms are also influenced by recurring orbits which are not periodic. This is due to the Coulomb singularity in atomic systems which has no counterpart in the billiard problems considered in [38].

Since in the experiments discussed in this paper Rydberg atoms are excited via transitions from a ground state localized at the Coulomb center, only wave-function enhancements generated by trajectories approaching the Coulomb center influence the excitation probability. This can be more directly seen from Eqs. (13) and (14), where only trajectories starting and ending at the Coulomb center contribute. Thus the average electric-dipole moments of the excited states should be connected to the dipole moments of recurring orbits which strongly modulate the spectrum.

There are different experimental possibilities to determine the electric-dipole moment of atoms. In ordinary Stark energy-level maps the atomic dipole moment is given by the slope of the level energy plotted versus the electric field $\frac{\partial W_n}{\partial E}$. However, for parameters used in the experiments presented in this paper the level density is very large (due to the high excitation energy and the hyperfine-structure splitting of the ground state). For that reason in most cases it is not possible to associate slope values $\frac{\partial W_n}{\partial E}$ with excited atomic states. But in analogy to the determination of electric-dipole moments from Stark energy-level maps it is possible to derive an electric-dipole moment from the shift of the QL structure in the spectra when changing the electric field. The obtained dipole values, which are a collective property of many electron states, coincide with the dipole moments of the classical orbits associated with the QL resonances (see Ref. [42]).

In this work we follow the more direct method of measuring the atomic dipole moments: The results of the dipole deflection experiments allow one to measure directly the charge separation in individual atomic states (see Sec. VI). Since individual wave functions may be influenced predominantly by one classical trajectory, the dipole deflection experiments are interpreted in Sec. VI by properties of classical trajectories modulating the excitation spectra and having large electric-dipole moments.

IV. QUASI-LANDAU MODULATIONS IN THE SPECTRA OF RYDBERG ATOMS IN CROSSED FIELDS

Since we want to interpret the appearance of large dipole moments by the properties of classical trajectories which influence the excitation spectra, some results concerning the QL resonances in the spectra of Rydberg atoms in crossed fields are presented. The largest dipole deflections were experimentally observed at the ionization energy, which essentially depends on the electric-field strength according to Eq. (1), and which is only slightly increased due to the additional magnetic field. Therefore all the Fourier transforms of scaled spectra shown in Fig. 4 are taken slightly below the ionization limit. Figure 4 demonstrates that it is possible to separate the excitation spectra into well-defined Fourier components, each corresponding to one or more classical trajectories. It turns out that especially the resonances labeled by C_i in Fig. 4 are associated with orbits which may exhibit extraordinarily large electric-dipole moments. Therefore these resonances will be discussed in what follows in more detail.

Figure 5 shows the C_i orbits for parameters corresponding to those of the Fourier spectra displayed in Fig. 4. The size of the scaled trajectory dipole moments δ_s [see Eq. (18)] and the squares α of the modulation amplitudes calculated according to Refs. [39, 40] are also given. The trajectory having the largest dipole moment is the C_0 orbit. However, below the ionization energy W_{ion}, which in Fig. 5 was chosen to be $\approx -50\ \mathrm{cm}^{-1}$, this trajectory exists only if the scaled electric field exceeds the value $\epsilon = 0.66$. For those parameters, however, the modulation amplitude of the C_0 orbit is rather low, and it may be possible only for parameters as in Fig. 4(e) that the C_0 orbit generates a weak QL resonance.

In all Fourier spectra shown in Fig. 4 the C_1 resonance shows up as one of the strongest resonances, except Fig. 4(a) and 4(c), where the C_1 orbit influences the excitation spectra relatively weakly. The low theoretical resonance strength for $\epsilon = 1.148$ explains why the C_1 resonance shows up so weakly in the experiment [Fig. 4(a)]. The relatively weak C_1 resonance in Fig. 4(c) at first glance contradicts the quite large theoretical resonance strength indicated in Fig. 5. However, the values given in Fig. 5 have to be compared to those valid for other types of trajectories which are of minor interest in this paper. For parameters corresponding to Fig. 4(c) the modulation strength of the C_2 resonance, for example, is larger than that of the C_1 resonance (see Fig. 5). Furthermore it was observed that the QL resonances show a specific ionization behavior: As the excitation energy approaches the ionization limit, the different QL resonances are attenuated differently by signal loss due to photoionization. For parameters corresponding to Fig. 4(c) the A resonance is attenuated less than the other QL resonances when approaching the ionization energy. This is the reason why the A resonance dominates the Fourier spectrum in Fig. 4(c).

In many Fourier transforms of scaled spectra, one resonance strongly dominates the Fourier spectrum; for example, the C_1 resonance dominates the spectrum Fig. 4(b). This effect is also encountered far below the ionization energy, thus it cannot be explained in general by the particular ionization behavior of QL resonances. The reason for that phenomenon becomes clear if the modulation strength associated with different orbits is considered as a function of the excitation energy. Figures 6 and 7 show the results obtained for the C_0 and C_1 trajectories. These data on the resonance strengths and corresponding plots for other orbits reproduce the observed strengths of the QL resonances reasonably well. The most outstanding feature of the plots in Figs. 6 and 7 is the appearance of pronounced maxima in the modulation strengths at certain energy values. These maxima are important with respect to the interpretation of the dipole deflection experiments. Detailed investigation of these peaks reveals that they are in fact singularities. Their nature can easily be seen in Fig. 8, where for parameters close to a singularity of the C_0 resonance strength several trajectories are depicted. It can be easily recognized that all trajectories leaving the core region within a certain angular range are focused back to the core region. In other words, the groups of trajectories have a focal line in the vicinity of the core region. In the formalism described in Refs. [39, 40] this fact leads to a very large modulation amplitude associated with that trajectory. Actually, if the focus of the trajectories lies on the surface on which the trajectories terminate, the modulation strength calculated according to Refs. [39, 40] becomes infinite. Although this infinity is, as mentioned in Refs. [39, 40], an artifact due to the failure of the lowest-order semiclassical approximation of the Green's

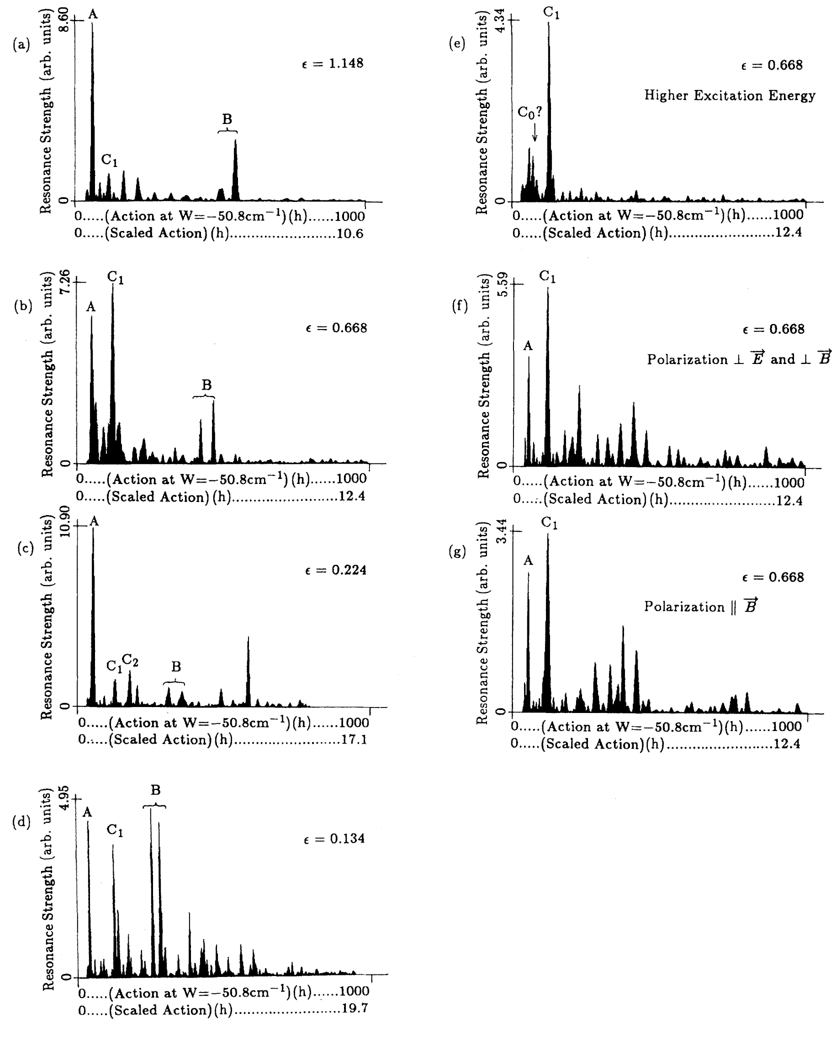

FIG. 4. Experimental Fourier spectra of scaled scans for different scaled electric-field strengths $\epsilon = EB^{-4/3}$ at the ionization energy and for laser polarization parallel to the electric field (a)–(e). The resonance A is caused by the simplest closed orbits of the system which are described in Ref. [42]. As the magnetic field is increased, i.e., as one moves from spectrum (a) towards (d), the perturbation of the atom increases more and more, and the resonance group B shifts to smaller action values. This is due to the fact that the trajectory type responsible for those resonances (which in Ref. [42] is called the 2 π trajectory) reduces in action as the magnetic field is increased. The resonances most important to this paper are labeled by C_i. The parameters of spectrum (e) are the same as in (b), except for a slightly increased excitation energy. Actually the average counting rate observed during the recording process of spectrum (e) was about 10% of that in spectrum (b). The main difference between (b) and (e) is that all QL resonances except the C_1 resonance disappear at the ionization energy, indicating that a specific ionization behavior of different QL resonances exists. Spectrum (e) may additionally exhibit a C_0 resonance. The spectra (f) and (g) are taken at the same parameters as (b) except for the laser polarization. Comparison between (b), (f), and (g) nicely demonstrates the polarization dependence of the QL resonances, which is described by the formalism of Du and Delos [39, 40]. The resonance strengths are normalized to the total counting rate in the particular experiments, i.e., it is possible to compare different plots in the figure quantitatively.

function close to conjugate points, the actual modulation amplitude becomes extraordinarily large for those parameters. How these focal lines, which enhance the resonance strength enormously, evolve as the scaled energy is changed is illustrated in the following examples.

In Fig. 9, where the scaled electric field is the same as in the spectrum of Fig. 4(b), one can clearly see three singularities. At the first one, which occurs at $W = -51\ \mathrm{cm}^{-1}$, the Maslov index increases by 1 with increasing W, corresponding to a new conjugate point along the orbit. Figure 9 shows that the new conjugate point emerging from the terminal surface is a focal line of the trajectory which is parallel to the magnetic field, i.e., the trajectory is focused in the ϕ_0 degree of freedom. As the energy is increased further, the modulation amplitude decreases, reflecting the increasing distance between the terminal surface of the trajectories and the focal line. At $W \approx -49\ \mathrm{cm}^{-1}$, however, the focus turns back and approaches the terminal surface again. At $W = -47.7\ \mathrm{cm}^{-1}$ it disappears again (the Maslov index changes by -1), thus producing another singularity as the focal line crosses the terminal surface of the trajectories. At an energy of $W = -44.9\ \mathrm{cm}^{-1}$ the Maslov index increases again by 1 since a new focal line emerges from the terminal surface of the trajectories. This focal line lies in the plane perpendicular to the magnetic

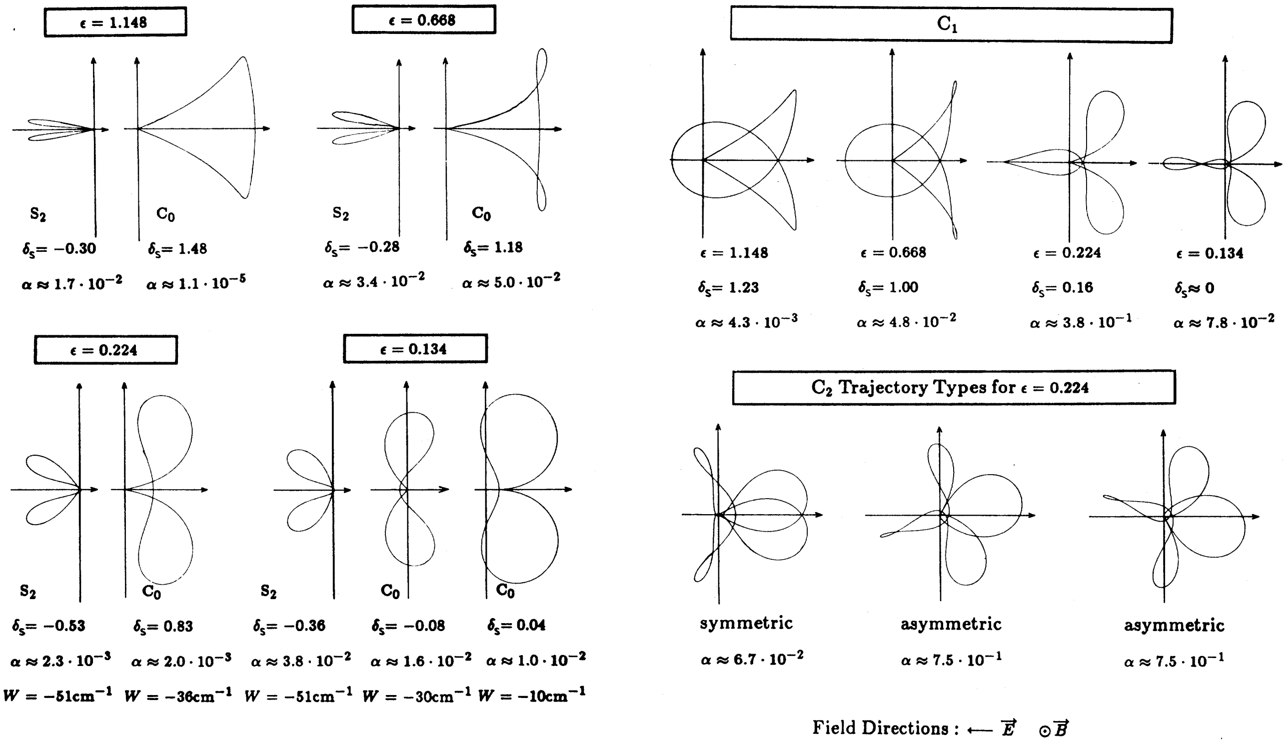

FIG. 5. Trajectories with large dipole moments for different scaled electric fields ϵ. If no energy value is indicated the trajectory is calculated for the ionization energy $W_{\mathrm{ion}} = -51\ \mathrm{cm}^{-1}$. For $\epsilon = 0.224$ and 0.134 the C_0 orbit is also shown for higher excitation energies (above the ionization limit) in order to show the evolution of the S_2 into the C_0 orbit. The figure also indicates the scaled dipole moments δ_s of the orbits [see Eq. (18)] and the modulation strengths α in the same units used in Figs. 6 and 7. For scaled electric fields $\epsilon < 0.7$ the C_0 orbit only exists for energies above the ionization limit, which are not accessible to the experiment discussed in this paper. It evolves continuously from the S_2 orbit, as shown for $\epsilon = 0.134$ and 0.224. There is no energy range where both orbits C_0 and S_2 coexist. For $\epsilon > 0.7$, the C_0 trajectory and the S_2 orbit, which are nearly degenerate in action, coexist within a certain energy range which covers the ionization energy. If a resonance at that action is observed, it is necessary to determine by classical stability calculations whether the S_2 or the C_0 orbit causes the resonance. Usually the modulation strength of the S_2 orbit is larger than the C_0 modulation strength. It must be mentioned that the value $\alpha \approx 5 \times 10^{-2}$ for the C_0 orbit for scaled electric field $\epsilon = 0.668$ is very unstable; if one of the parameters W, E, or B is slightly changed the C_0 modulation strength rapidly drops (see also Fig. 6). The C_1 trajectory exists at the ionization energy over the whole examined scaled electric-field range. In comparison with other trajectories it exhibits a large resonance strength leading to a quite dominant signal in the Fourier spectra. The C_2 trajectory is depicted for $\epsilon = 0.224$, where it modulates the spectrum stronger than the C_1 orbit. For the orbits C_i not only the symmetric orbit type exists, but also asymmetric types with nearly equal action, each having a certain complex modulation amplitude. As an example, the three C_2 orbit types are depicted at the bottom of the figure (see also Fig. 8). The total resonance strength is obtained by taking the square of the modulus of the complex sum over the individual modulation amplitudes of all trajectories having the same action.

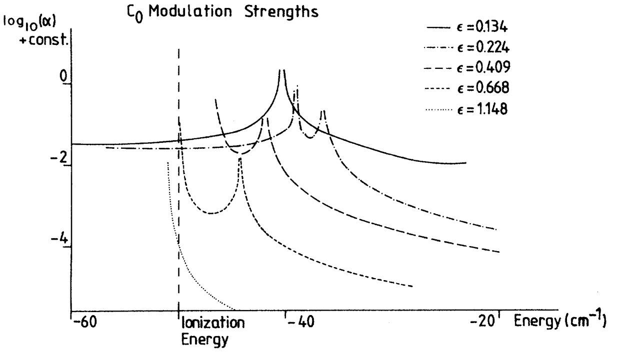

FIG. 6. Resonance strengths of the C_0 orbits for different scaled electric fields. The plotted values in Figs. 6 and 7 do not include the influence of the laser polarization (although can easily be calculated) since in this paper the major interest is in the intrinsic classical stability behavior of the orbits. The left-hand parts of the curves for $\epsilon = 0.134$ and 0.224 actually are modulation strengths of the S_2 trajectory, which evolves continuously into the C_0 orbit as the energy is increased. As in Figs. 7, 11, and 12 the ionization energy is indicated by a broken vertical line.

field and corresponds to the focusing in the θ_0 degree of freedom.

A kind of limiting case occurs in Fig. 7 for $\epsilon = 0.409$, where instead of a singularity, a smooth bump appears at an energy of $W \approx -48$ cm^{-1}. Figure 10 illustrates that as the energy approaches that value from any side, a virtual focus in the ϕ_0 coordinate (labeled in Fig. 10 by a v) approaches the terminal surface of the trajectories, but does not reach it. Therefore no singularity occurs, only a bump.

Now we turn to the dipole moments of the trajectories which are displayed in Figs. 11 and 12. It can clearly be seen that large trajectory dipole moments and large modulation amplitudes coincide at a scaled electric field $\epsilon \approx 0.7$ in the vicinity of the ionization energy. Fig-

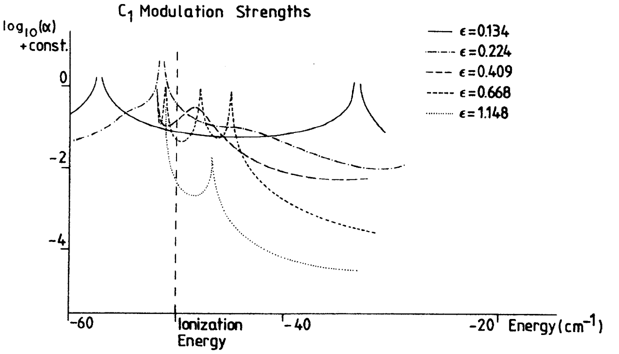

FIG. 7. Resonance strengths of the C_1 orbits for different scaled electric fields. Similarly to Fig. 6 at low scaled electric fields there is a continuous transition between the C_1 orbit and another trajectory with negative dipole moment.

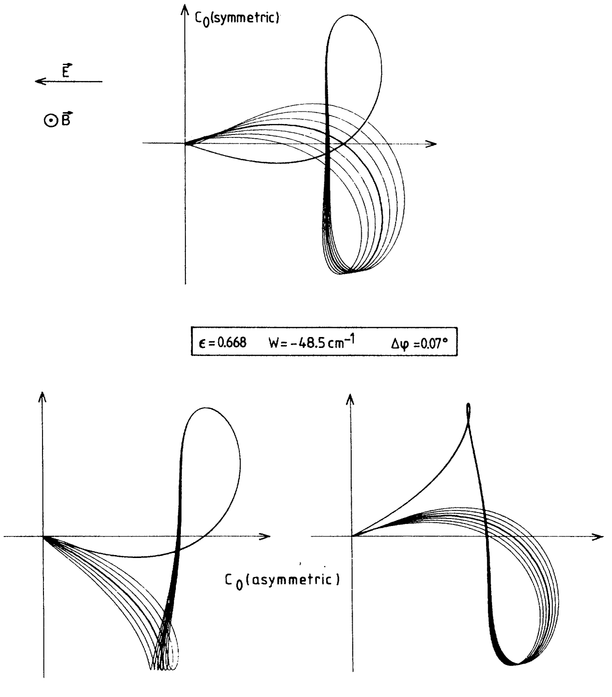

FIG. 8. Visualization of the resonance strength maximum of the C_0 orbit encountered at $W \approx -48.5$ cm^{-1} and $\epsilon = 0.668$. At those parameters the symmetric type as well as the asymmetric types of C_0 orbits cause focusing back to the core region. This is demonstrated by launching trajectories in several directions (here differing by 0.07°) close to the central trajectory, which returns with zero angular momentum and which is enhanced in the figure.

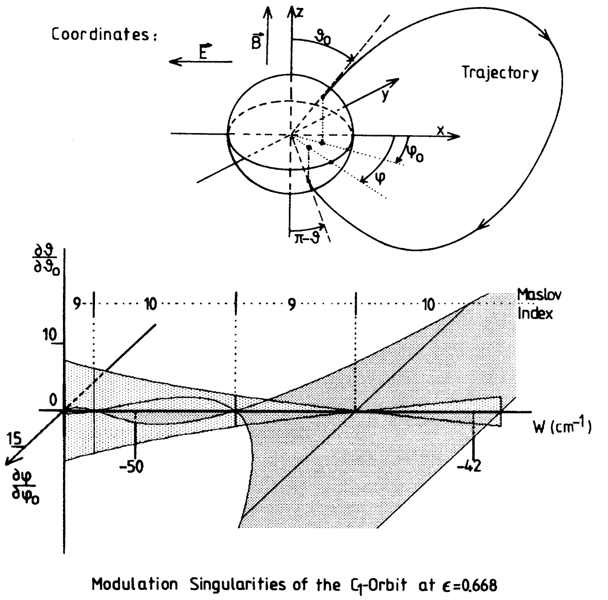

FIG. 9. Stability behavior of the C_1 orbit at $\epsilon = 0.668$. The resonance strength is approximately proportional to the inverse product of $\frac{\partial\theta}{\partial\theta_0}$ and $\frac{\partial\phi}{\partial\phi_0}$, leading to a singularity if the trajectory is focused back to a line in the θ or ϕ directions. As also indicated on the figure, the Maslov index changes by 1 if a singularity is passed.

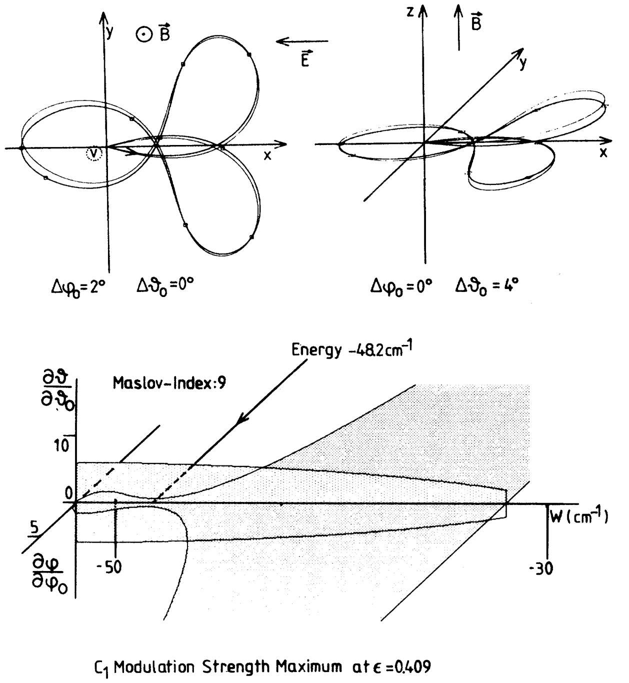

FIG. 10. Stability behavior of the C_1 orbit at $\epsilon = 0.409$. As is clear from Fig. 9 the modulation maximum of the C_1 orbit at $W \approx -47\ \mathrm{cm}^{-1}$ is due to the minimum of $\frac{\partial\phi}{\partial\phi_0}$ at that energy. The upper part of the figure shows that there are different conjugate points (labeled by small squares in the figure) determining the Maslov index: the left pair of trajectories consists of the central trajectory (bold) and a neighboring trajectory differing only in ϕ_0. It can be seen that there are four foci and one caustic in the plane perpendicular to **B**. The three-dimensional plot in the upper right of the figure shows the central trajectory (bold) and a trajectory differing only in θ_0. One can recognize four foci in the **B** direction.

ures 4(b) and 4(e), which are taken at these parameters, exhibit a strong C_1 resonance in agreement with the quite large theoretical modulation strength given in Fig. 5. As can be seen from Fig. 12 the dipole moment of the C_1 trajectory decreases rapidly as the scaled electric-field strength is reduced. On the other hand, as the scaled electric field is increased, the modulation strength related to the C_1 orbit decreases far below the values associated with competing QL resonances. Therefore the C_1 orbit is expected to favor atomic states with large dipole moments for a scaled electric field of $\epsilon \approx 0.7$. As shown above (Fig. 9) for this value of the scaled electric field the modulation amplitude of the C_1 resonance is extraordinarily enhanced by three focal lines which successively hit the terminal surface of the trajectories when the excitation energy is varied around the ionization energy.

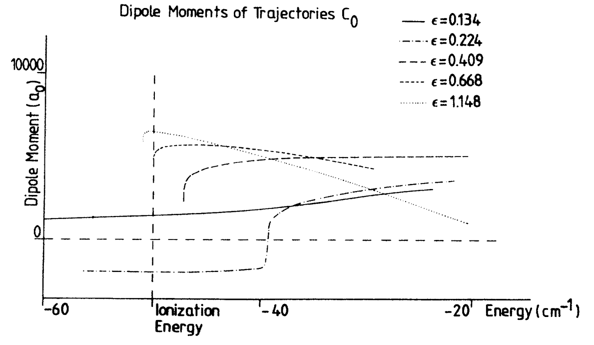

FIG. 11. Dipole moments of the trajectories belonging to the C_0 orbit.

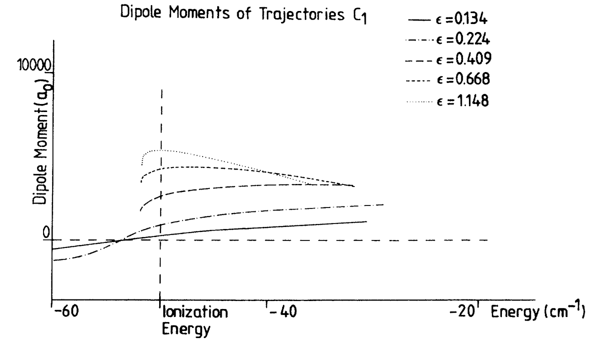

FIG. 12. Dipole moments of the trajectories belonging to the C_1 orbit.

Similarly Fig. 6 shows that at the ionization energy the C_0 orbit exists only for $\epsilon > 0.7$. The corresponding QL resonance, however, may be observable only in a narrow range on the scaled electric-field scale since the modulation amplitude rapidly decreases as ϵ is increased from $\epsilon = 0.7$ (see Fig. 6). Only the $C_0(?)$ resonance in Fig. 4(e) may be due to the C_0 orbit. Despite the small C_0 resonance strength at $\epsilon \approx 0.7$ a few atomic states may be accidentally scarred by the C_0 orbit.

From the discussion of the QL resonances it can be concluded that atomic states with large dipole moments should occur for $\epsilon \approx 0.7$ in the vicinity of the ionization limit. Wave functions having large dipole moments should be influenced in the sense of Eq. (15) by the trajectories C_1 and perhaps C_0.

V. EXPERIMENTAL SETUP

The experimental setup is shown in Fig. 13. The experiments have been performed with rubidium Rydberg atoms, since these are much simpler to investigate than hydrogen atoms. The only difference compared to hydrogen is the modified potential close to the nucleus caused by the influence of the core electrons. The core potential does not affect the considerations with regard to the expected dipole moments of the atoms. Also the QL resonance structure which allows one to find the classical trajectories influencing the system is not changed significantly, as has been shown by O'Mahony for different alkali atoms in strong magnetic fields [53].

The atomic beam effuses from an oven having a temperature of about 630 K. The velocity of the atoms follows a modified Maxwell distribution or a supersonic distribution, depending on details of the oven (for example,

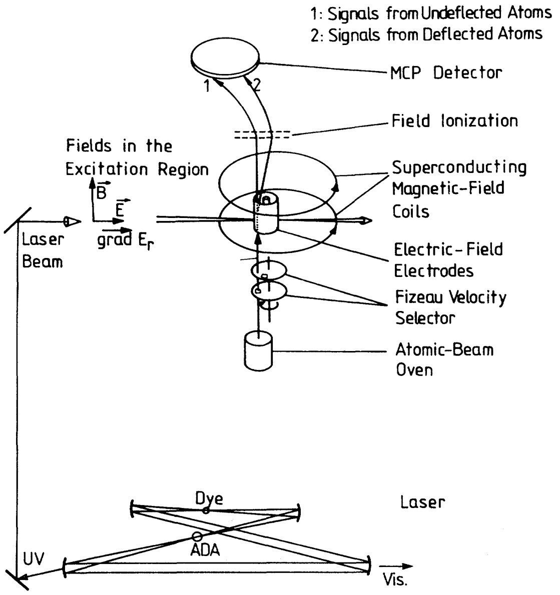

FIG. 13. Experimental setup. The velocity-selected Rydberg atoms are excited by a rhodamine 6G dye laser which contains a frequency-doubling ammonium dihydrogen arsenate (ADA) crystal at an auxiliary focus of the laser cavity providing the uv radiation. After the deflection the Rydberg atoms are field ionized. The field electrons are detected with a position-sensitive microchannel-plate (MCP) detector.

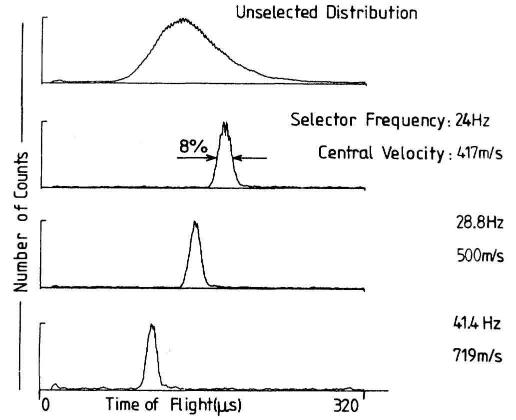

FIG. 14. Demonstration of the performance of the velocity selector. The time-of-flight distributions prove that there is no slow velocity sideband leading to a group of strongly deflected atoms and thus simulating large dipole moments. Thus it is ensured that the observed large deflection of a part of the atoms must be due to their large electric-dipole moment.

the nozzle diameter). Since the dipole deflection depends on the atomic velocity ($\sim v^{-2}$) the atomic beam must be velocity selected. This was achieved by a mechanical velocity selector consisting of ten slotted disks mounted with well-defined spacings and torsion angles on a motor driven axis. The velocity selected beam has a full width at half maximum of 8%. Owing to the small number of strongly deflected atoms the velocity distribution of the atoms should not exhibit side maxima at small velocities. This is shown in Fig. 14, where time-of-flight data on the velocity distribution are displayed. The relative transmission ratio in the center of the selected velocity band was close to 0.5.

The excitation of the rubidium Rydberg levels was performed by the frequency-doubled radiation of a dye laser (rhodamine 6G). The interaction region between laser and atomic beams is located in the middle of the electrode arrangement producing the electric field and in the homogeneous part of the magnetic field. The laser beam crosses the atomic beam at right angles. The residual Doppler width amounts to 15 MHz. In order to avoid a motional electric field ($\mathbf{v} \times \mathbf{B}$ contribution) the magnetic field which is generated by a superconducting pair of coils must be parallel to the atomic beam. The electric field can be chosen to be homogeneous, as needed for spectroscopic measurements, or to be slightly inhomogeneous, as necessary for dipole-deflection measurements. The geometry of the six electrodes used to produce the electric field is shown in Fig. 15. The three voltages V_0, V_1, V_2 are connected to the electric-field strength and its first and second derivatives in the x direction (see Fig. 15) at the center of the arrangement. The voltages which have to be applied in order to get certain fields and inhomogeneities (the second derivative was usually set to zero) can be easily calculated via a system of linear equations.

About 200 μs after the excitation, all Rydberg atoms

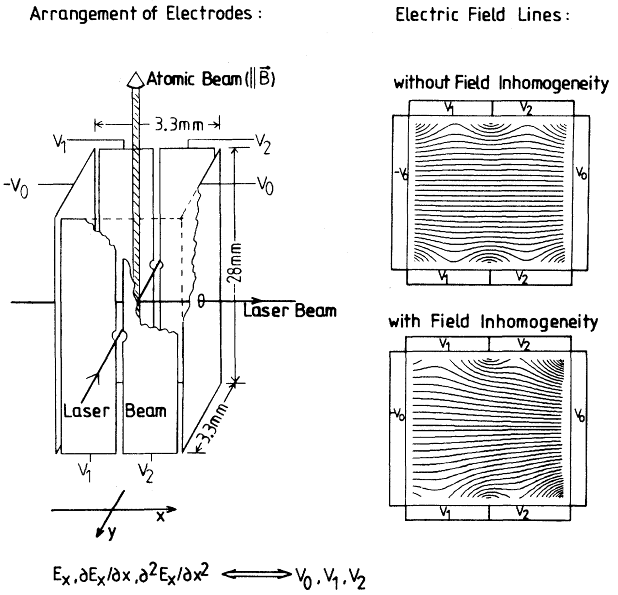

FIG. 15. Electrode arrangement producing the electric field. Using the three potentials V_0, V_1, and V_2, arbitrary field values and field inhomogeneities can be chosen. Since the electrodes are very long in comparison to their separation the electric field drops to zero within a small distance on the z scale, providing well-defined conditions during the deflection process.

are field ionized, and the stray magnetic field deflects the field electrons onto a microchannel-plate (MCP) detector. The ionization field and the magnetic-field strength have to fulfill certain conditions to guarantee that the image of the atomic beam is not distorted and smeared out by drift effects occurring in electric and magnetic fields.

Since the dipole moments are deduced from the dipole deflection the atomic beam image in the detector plane must be well defined; thus the spread of the atomic beam due to its own divergence and diameter must be minimized by using good collimation. This is also necessary in order to achieve the optimum performance of the velocity selector. Furthermore the spread of the electric field across the atomic-beam diameter must be kept small. All these precautions have to be taken without diminishing the average counting rate significantly in order to keep the integration time and the fraction of dark counts within reasonable limits. Taking these considerations into account the experimental parameters were set in a manner allowing measurements of atomic dipole moments with an accuracy of about 25–30 %.

The laser frequency, the voltages determining the electric field, and the magnetic field are controlled by a computer which is also used to integrate the signal counts for the ordinary or scaled spectra, and to sample the two-dimensional images produced by the microchannel plate. Different evaluation programs were used to Fourier transform the spectra, yielding the revolution times or action values of the orbits influencing the spectra. In addition, the programs were used to perform operations on the atomic beam images, for example, averaging and rotating, necessary to prepare the images for the evaluation of the atomic dipole moments.

VI. EXPERIMENTAL RESULTS

Before the results of the dipole deflection measurements are presented and discussed it is necessary to understand what is measured in the experiment. The simplest model would be to assume fixed dipole moment, field inhomogeneity and velocity of the atoms. In that case the electric-dipole moment d could be calculated from the observed deflection Δx in the following way:

$$d = \frac{M}{\left(\dfrac{\partial E_x}{\partial x}\right)[(L_1^2/2) + L_1 L_2]} \Delta x \, v^2 \tag{16}$$

with atomic mass M and velocity v (Δx, L_1, L_2 are explained in Fig. 16). However, the assumption of a fixed dipole moment is not necessarily fulfilled. During the time the atom passes through the apparatus the following events take place:

(i) An atomic state is excited by the laser within well defined crossed fields at time $t = 0$ (location 1 in Fig. 16).

(ii) The Rydberg atom experiences a force $\mathbf{F}(t) = \nabla[\mathbf{d}(t) \cdot \mathbf{E}(t)]$ and is accelerated. It is a good approximation to consider only the x component of the motion, $F_x(t) = \frac{\partial E_x}{\partial x} d(t)$. The field inhomogeneity can be assumed to be constant. The electric field acting on the Rydberg atom, however, changes as a function of time, thus the electric-dipole moment determining the deflection force also changes according to the energy-level map.

(iii) The Rydberg atom reaches level crossings (and anticrossings). The levels accidentally cross (Poisson statistics) or repel each other, as observed in classically chaotic quantum systems. Depending on that behavior, the atoms prefer the diabatic or adiabatic passage, respectively (location 2 in Fig. 16).

(iv) At a time T the atoms pass a region in which the electric field is switched off as fast as possible, i.e., the electrodes are designed so that the error due to uncontrolled deflection is minimized (location 3 in Fig. 16).

(v) The atoms reach the detection zone with a deflection Δx which is proportional to the momentum kick they experienced due to the electric-dipole force (location 4 in Fig. 16).

Thus the quantity which can be derived from the measured deflection Δx is

$$\bar{d} = \frac{1}{T} \int_{t=0}^{T} d(t')dt' \,, \tag{17}$$

i.e., the average dipole moment the atom takes as the deflection process goes on is measured. This implies two important conclusions:

(i) The actual maximum value of the electric-dipole moment d is larger than the measured one.

(ii)The measured dipole moment depends on the path the atom takes in the level scheme. An entrance space distribution of excited atoms $W_{\text{in}}(\Delta x)$ is mapped onto a distribution $W_{\text{out}}(\Delta x)$ in a way governed by the level scheme and the Landau-Zener formula.

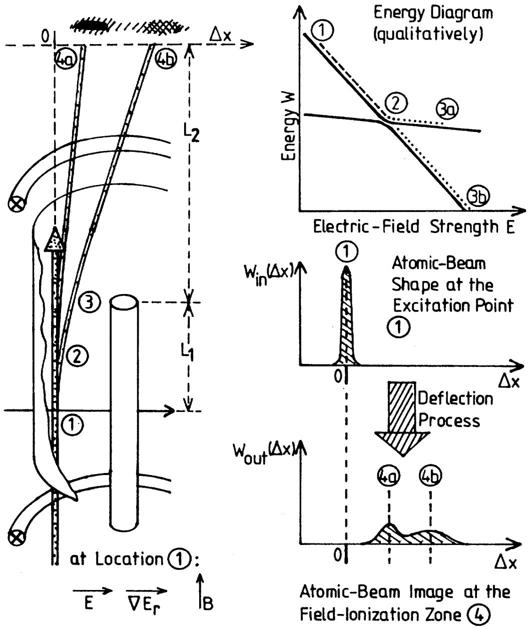

FIG. 16. Investigation of the deflection process. For simplicity the structure of the electric field is not the same as in Fig. 15. The figure shows that due to the dynamical character of the deflection the observed deflection patterns only allow one to determine an average dipole moment, not $\frac{\partial W_n}{\partial E}$ for the excited energy eigenstates. The average dipole moment depends on the level-crossing behavior at point 2.

The simplest method to decide whether the atoms pass diabatically or adiabatically is to measure the dipole deflection as a function of the field inhomogeneity, i.e., the range in the level scheme relevant for the deflection is changed. The result of such a measurement done with $E = 17\,000$ V/m, $B = 0.7$ T, and excitation energy close to the ionization limit is displayed in Fig. 17. The observed proportionality between deflection and field inhomogeneity allows one to conclude that the atoms perform a diabatic passage.

Since the knowledge of the passage behavior is a crucial point in this work, another type of measurement to answer that question was performed. We measured the dipole deflection at constant electric field and constant excitation energy just below the ionization limit as a function of the magnetic field in the range from 0 to 3 T. The obtained deflection patterns are shown in Fig. 18. It can be recognized that the dipole deflection of the atoms starts with quite large values at low magnetic fields. As the magnetic field is increased the dipole deflection passes a minimum, then rises to a maximum, and decreases again at very high magnetic fields. It is known from the literature [54] that at excitation energies used for the measurements shown in Fig. 18 and an electric field $E = 0$ the classical dynamical behavior of the electron becomes gradually chaotic in magnetic-field ranges of $B = 0.8$–3 T and $B = 2.0$–7.4 T, corresponding to the left and right columns of Fig. 18, respectively. Provided that similar magnetic-field values are valid if the electric field is added, it might be concluded that due to the level repulsion in classically chaotic quantum systems at the right end of the deflection patterns shown in Fig. 18, predominantly adiabatic passage takes place (labeled by 3 in Fig. 18). The expected deflection pattern would give quite large dipole moments, since in the level scheme the atom would pass a considerable number of "steep" paths. In a transition region between diabatic and adiabatic passage, strong fluctuations in the observed dipole moments should occur since there should be comparable fractions of atoms passing diabatically and adiabatically. The maximum in the standard deviations of the dipole deflection at magnetic-field values labeled by 2 in Fig. 18 can be explained by such a transition. For lower magnetic fields (region 1) atoms should predominantly pass diabatically. In general it must be expected that the oscillator strengths of states exhibiting low dipole moments are larger than those of high dipole moment atoms. Since in the diabatic-crossing regime the average dipole moment during the deflection is essentially determined by the dipole moments of the atoms immediately after excitation, we expect quite small dipole deflections in the diabatic regime (region 1). Thus the observed decrease of dipole deflection as the magnetic field changes from region 2 to 1 can be explained by a decreasing fraction of atoms altering their initially rather low dipole moment to a large one via adiabatic passages.

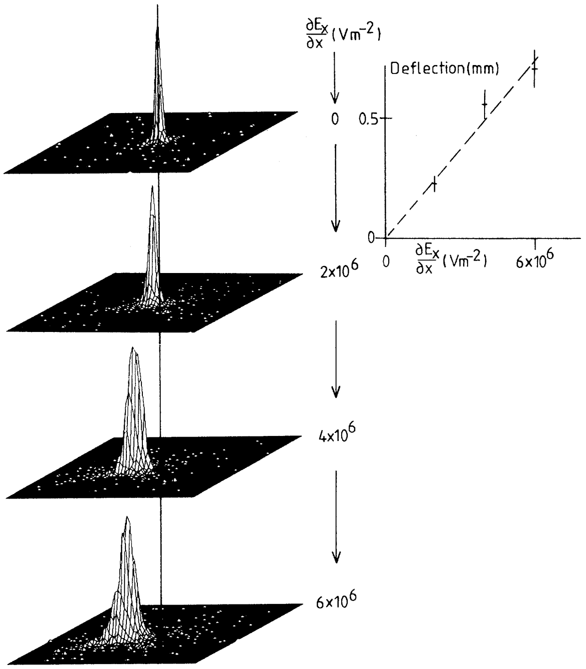

FIG. 17. Dipole-deflection patterns at $B = 0.7$ T, $E = 17\,000$ V/m, and $W = -80$ cm^{-1}, which is close to the ionization energy. The deflection at point 3 (Fig. 16) amounts to about 0.13 mm for $\frac{\partial E_x}{\partial x} = 6 \times 10^6$ V/m^2, corresponding to an electric-field change of about 800 V/m. Knowing the dipole moment of about $250e\mathcal{A}$ (see below), where $\mathcal{A}$=1 Å, the energy change of the atom during the deflection turns out to be about 0.15 cm^{-1} = 4.5 GHz. As is clear from excitation spectra taken in this parameter region, the number of levels coupled to the ground state within that energy range is at least on the order of 50; thus it follows that the atom passes a large number of level crossings during the deflection process. The observed proportionality between $\frac{\partial E_x}{\partial x}$ and the deflection shows that the dipole moment of the atom does not change dramatically during the deflection, thus the level crossings are passed diabatically.

The features observed in Fig. 18 can be explained by assuming a change of the crossing behavior from diabatic to adiabatic. Particularly for the scaled electric field $\epsilon \approx 0.7$ at the ionization limit we expect that the atoms prefer to cross diabatically during the deflection process, resulting in measured dipole moments which should not deviate much from the actual atomic dipole moments immediately after the laser excitation. It should be mentioned that the conclusions from Fig. 18 are drawn from the behavior of the majority of the atoms, which exhibit relatively small dipole deflections. The reason Fig. 18 exhibits no strongly deflected atoms, as found in the measurements which follow below, is simply that in Fig. 18 they would appear at magnetic field values as small as $B = 0.16$ and 0.38 T, respectively. At low magnetic fields, however, the applied imaging technique from the field ionization zone onto the MCP does not operate well enough to separate the strongly deflected atoms from the dominating fraction of weakly deflected atoms. However, if the weakly accelerated low dipole moment atoms pass diabatically, then the strongly accelerated high dipole moment atoms do so as well.

The atomic-beam images presented in Fig. 19 are the most important results obtained by the dipole-deflection method. The measured deflection distance allows one to calculate the average electric-dipole moment during the deflection according to Eq. (16). So that the results for different excitation energies can be compared to each other it is convenient to calculate the scaled electric-dipole moment d_s given by

$$d_s = d|W| \tag{18}$$

with energy W and electric-dipole moment d in atomic units. d_s describes the charge separation distance between the nucleus and the electron in units of $1/|W|$, which under field-free conditions is the maximum distance between a classical electron and the nucleus at energy W. To get a feeling for the size of d_s we note that an electron localized at the classical ionization saddle point would have a scaled electric-dipole moment $d_s = 2$. In Fig. 19 the axis showing the deflection distance is transferred into a scale giving the scaled electric-dipole moment. Figure 19 shows the observed deflection patterns at energies of -90.5, -78.5, and $-69.7\ \mathrm{cm}^{-1}$. The velocity of the atoms selected by the Fizeau velocity selector is indicated on top of the three columns. The uppermost pattern in each column shows the undeflected beam, which is obtained by switching off the field inhomogeneity. In all of the following dipole-deflection patterns the scaled electric field was tuned to the ionization limit in order to obtain the largest dipole deflections. The scaled electric field values are indicated in Fig. 19 together with the magnetic field on the left-hand side of the pictures. The unscaled electric-field strength in atomic units can be calculated by $E = \epsilon B^{4/3}$, B taken also in atomic units. As the magnetic field increases, the unscaled ionizing electric field strength also slightly increases, indicating that the magnetic field slightly increases the stability of the atoms with respect to ionization. However, it was observed that at a certain magnetic-field value larger than those applied in the experiments shown in Fig. 19 the ionization electric-field strength drops again.

Now we discuss the dipole deflection shown in Fig. 19. First the behavior of the central peak is examined, this corresponding to the main body of the atoms considered also in Fig. 18. As the magnetic field is increased, the

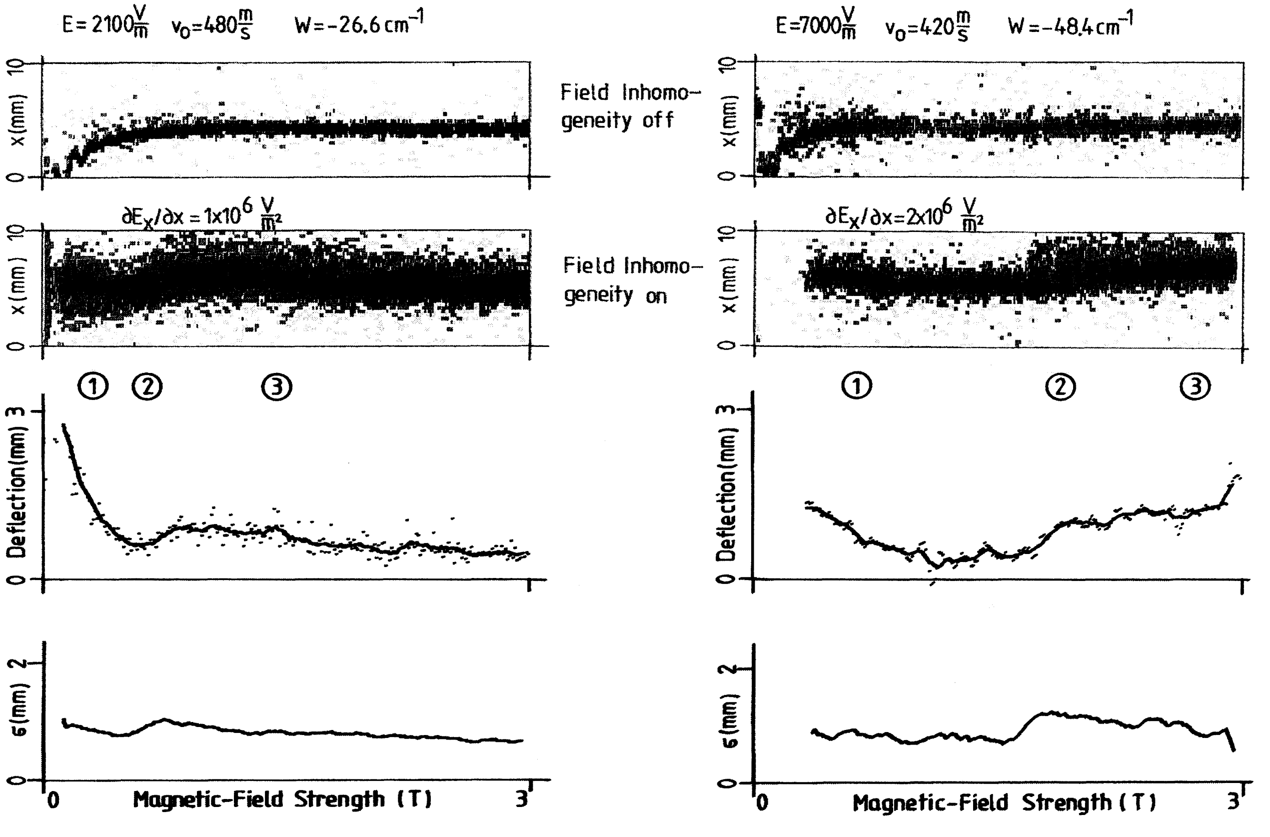

FIG. 18. Dipole deflection at the location of the MCP as a function of the magnetic field for constant electric field and excitation energy close to the ionization energy (two measurements). The number of counts in the pixels increases from yellow to black in a logarithmic scale. The upper images are taken without electric field inhomogeneity, the lower ones with the indicated values of the field inhomogeneity. The deflection as a function of the magnetic field is obtained by subtracting the zero-inhomogeneity atomic-beam position from the average location with applied field inhomogeneity (dots). The solid curve gives the deflection averaged over ten pixels on the B axis. The standard deviation σ is obtained by evaluating the deflection distribution $N(x, B)$ for each magnetic-field value B with respect to x. The interpretation of the increase of the deflection and the standard deviation at certain magnetic-field values is given in the text.

deflection and thus the scaled electric-dipole moments are reduced. This can be easily seen in Fig. 20, which contains the evaluated data of Fig. 19. The decrease of the dipole moments with increasing magnetic field is the expected behavior since the first guess is that the diamagnetic potential should reduce the extension of wave functions perpendicular to the magnetic-field direction. Especially in classical trajectory calculations it can clearly be seen that at larger magnetic fields, trajectories starting at the Coulomb center extend less in the plane perpendicular to the magnetic field.

Now we turn to the strongly deflected atoms. It is not as easy as in the case of the central peak atoms to associate a dipole moment with them, because their number is relatively small and the broadening of the deflection value amounts to about 30%. The reasons for the total deflection broadening are the residual velocity spread (ca. 8%) leading to a relative deflection spread of about 17%, and the spread of the undeflected pattern (ca. 0.2 mm at the field ionization zone) which is due to the diameter of the laser beam at the excitation point, the divergence of the atomic beam, and the imperfections of the imaging process from the field ionization zone onto the MCP surface. The latter spreading mechanism especially reduces the image quality at low magnetic fields. Due to the large deflection spread even atoms with a fixed large dipole moment lead to a broad, weak deflection signal

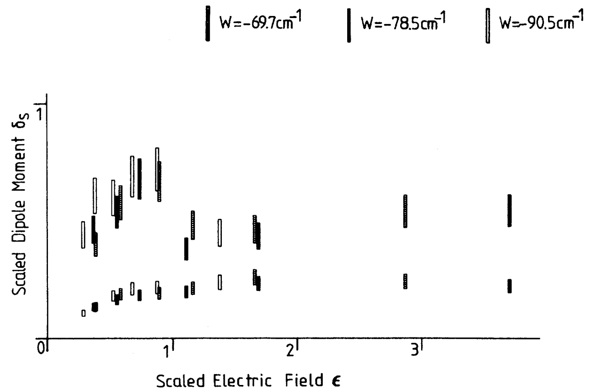

FIG. 20. Evaluation of the deflection data (Fig. 19). The three sets of measurements are distinguished by the bar structure. The error in the ϵ direction is negligible, the error of the average scaled dipole moment amounts to about 25% mainly due to the velocity spread of the atoms. Each deflection pattern of Fig. 19 corresponds to two bars: one bar indicating the average dipole moment of the main part of the atoms (black regions in Fig. 19) and one bar associated with the atoms showing the strongest deflection. The outstanding features of the plot are that the deflection of the central maximum increases with ϵ, and that strongly deflected atoms are found for $\epsilon \approx 0.75$.

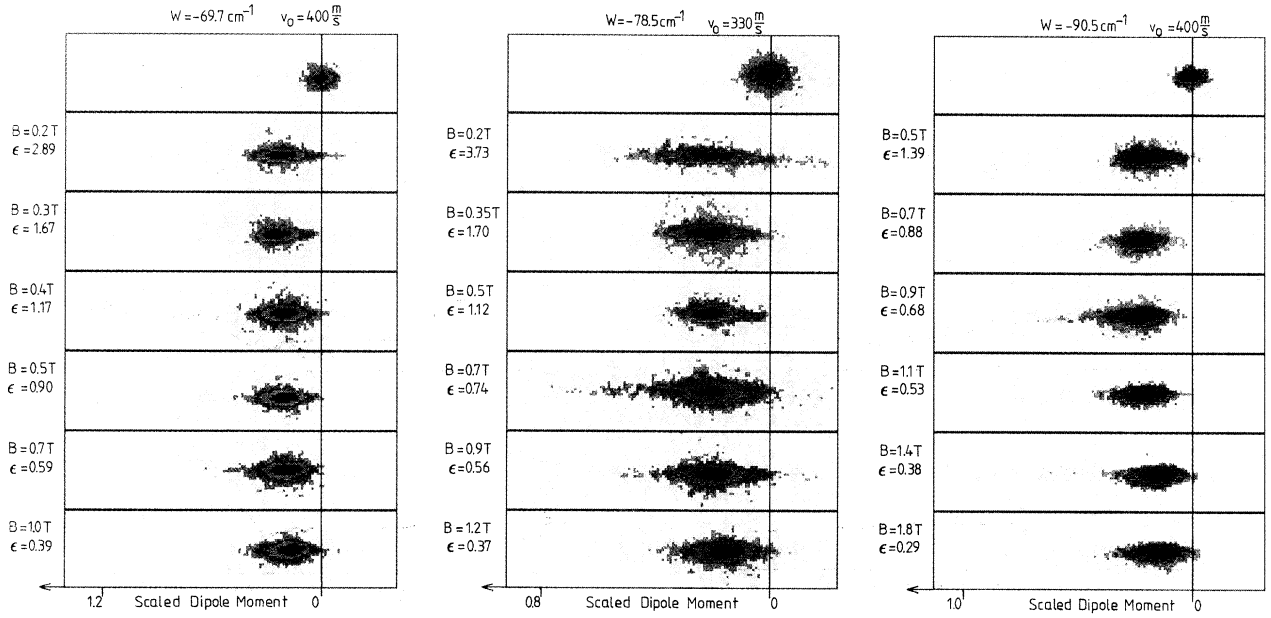

FIG. 19. Three sets of measurements showing the dipole-deflection pattern as a function of the scaled electric field at constant excitation energy, each image taken at the ionization limit. The images show the color-coded two-dimensional deflection patterns on the MCP surface, the color code being normalized to the maximum count number per pixel. The number of detected atoms increases from yellow to black in a logarithmic scale: one color covers a range of 0.477 on the $\log_{10}(n_{(x,y)})$, where $n_{(x,y)}$ is the number of counts in pixel (x, y). The uppermost row of images gives the reference position of the undeflected beam. If a field inhomogeneity is applied, the atoms are deflected in the opposite direction to the electric field, which is directed from left to right. The x axis gives the scaled electric-dipole moment following from the deflection value. It must be emphasized that this value corresponds to the average dipole moment of the atom during the deflection process (see Eq. 17).

which can only be separated from the broadened central peak if the deflection exceeds a certain value.

The mentioned difficulties lead to rather large error bars for the measured dipole moments of the strongly deflected atoms in Fig. 20. In spite of this, a clear statement can be drawn from the measurements: The dipole moment as a function of the magnetic field has a pronounced maximum in all three series at $\epsilon \approx 0.75$.

Since the relative number of strongly deflected atoms is small, we performed another experiment to check our interpretation of the observed deflection patterns. For this purpose the frequency of the laser was tuned over a convenient range, and the dipole deflection was plotted versus the frequency. Thus a two-dimensional image is achieved. Figure 21 shows the experimental results for three different scaled electric fields, corresponding to scaled electric fields above, at, and below the value resulting in maximum dipole deflection. For a laser scan width of $\approx 1.8\ \mathrm{cm}^{-1}$ the excitation spectrum corresponding to the total counting rate which follows from the color coding in Fig. 21 shows several maxima indicating short-scale QL resonances. The overall decrease in the counting rate as the laser frequency increases indicates the neighborhood of the ionization limit. The upper two measurements in the left column of Fig. 21 use a larger value for the inhomogeneity of the electric field (3×10^6 V/m^2); therefore the dipole scale is different from the others, where the inhomogeneity is 2×10^6 V/m^2. The following observations are made from Fig. 21:

(i) At scaled electric-field values above the one with maximum dipole deflection no strongly deflected atoms are observed (upper measurement in the right column of Fig. 21).

(ii) For scaled electric fields well below that value quite a large number of deflected atoms appear (lower measurement in the right column of Fig. 21). The corresponding dipole moments are moderate, in agreement with Fig. 20. It can also be observed that the number of deflected atoms is not correlated with the intensity of the central part of the deflection pattern, proving that the signal due

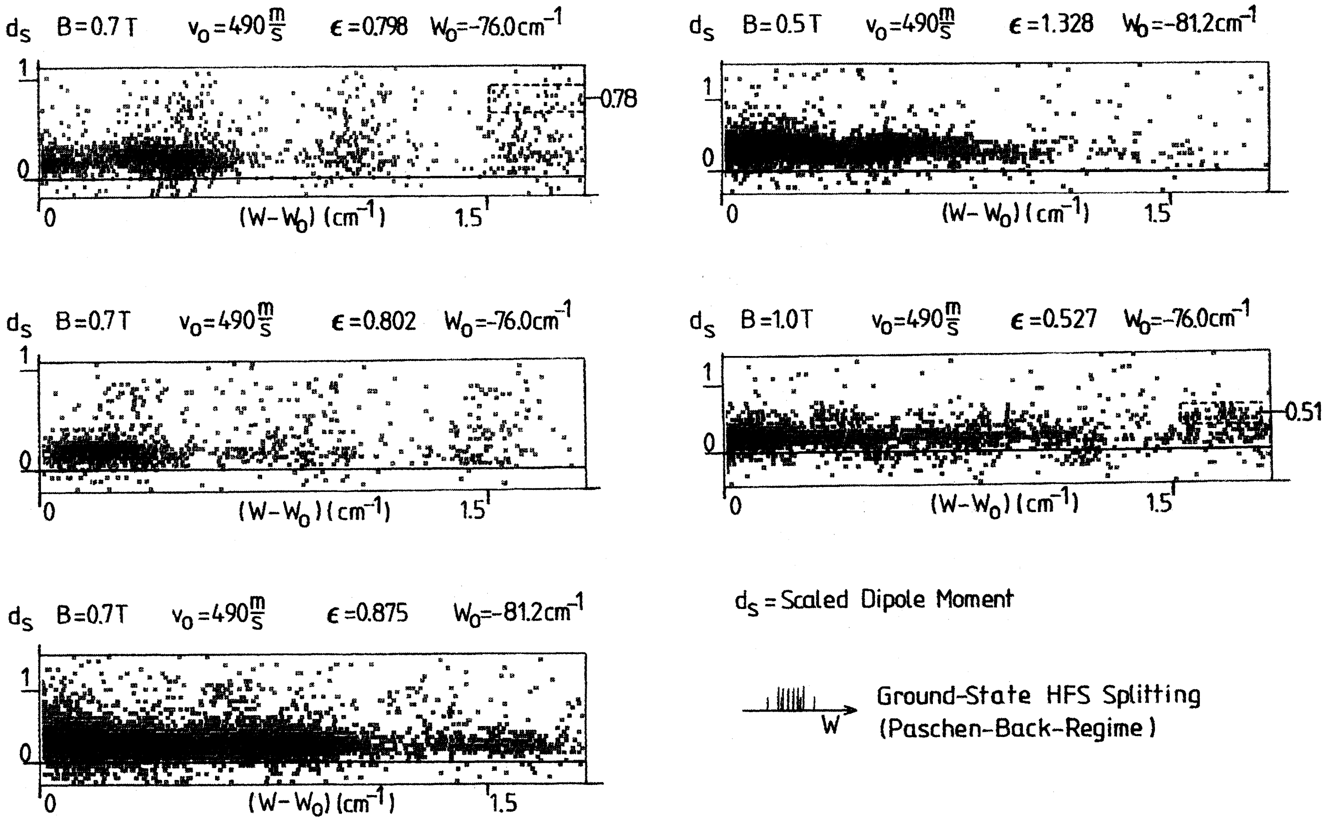

FIG. 21. Scaled average electric-dipole moments as a function of the excitation energy W for different scaled electric fields (color-coded images: the number of detected atoms increases logarithmically from red to black, one color covering a range of 0.477). The deflection spectra are taken very close to the ionization limit. At the large scaled electric field no strongly deflected atoms occur. For $\epsilon = 0.53$ (right column, lower picture) a fairly high fraction of moderately deflected atoms appears. For $\epsilon \approx 0.8$ a few atoms are strongly deflected (left column), the relative number clearly increasing with increasing energy. The width of the bunches of strongly deflected atoms on the energy scale coincides with the width of the ground-state Paschen-Back pattern of the hyperfine structure, being shown in the figure with the same energy scale as the deflection patterns. Some groups of strongly deflected atoms are not correlated with a large counting rate for weakly deflected atoms. This independent behavior ensures that the signals for strongly deflected atoms are not just caused by noise.

to the strongly deflected atoms is not the result of atoms in the wings of the spatial distribution for the weakly deflected atoms.

(iii) For the situation with maximum dipole deflection we show three measurements (left column in Fig. 21), all exhibiting a reasonable fraction of strongly deflected atoms. The scaled dipole moments which follow agree quite well with the other experiments shown in Figs. 19 and 20.

(iv) At several locations in the left column of Fig. 21, strongly deflected atoms appear where the number of weakly deflected atoms is small. This demonstrates again that the strongly deflected atoms are not correlated with the central maxima.

(v) The strongly deflected atoms appear in bunches having a width on the energy scale of $0.25 \pm 0.07\ \mathrm{cm}^{-1}$. This is clearly due to the ground-state hyperfine-structure splitting which in the Paschen-Back regime encountered in our measurements corresponds to a B-independent splitting pattern with $0.17\ \mathrm{cm}^{-1}$ width (see also Fig. 21). Thus one bunch of strongly deflected atoms should essentially correspond to one electronic state.

The presented data should convince the reader that the strongly deflected atoms really correspond to atoms exhibiting extraordinarily large dipole moments. In the following we give a semiclassical explanation of the strongly deflected atoms. The dipole-deflection maximum occurs for all experiments at the same scaled electric field ($\epsilon \approx 0.75$) and the same scaled energy ($\omega \approx -1.7$), therefore a semiclassical interpretation of the phenomenon should be possible. (The scaled parameters are derived from the classical Hamiltonian and are therefore intrinsically classical variables. The quantum Hamiltonian does not allow a similar scaling.) As explained in Sec. III we expect that the wave functions are influenced by classical trajectories. In order to interpret the appearance of the large dipole moments we must consider the QL orbits which were found to influence the excitation spectra and which exhibit large dipole moments. By comparing the experimental results just presented and the results concerning the modulation strengths and dipole moments presented in Sec. IV it is found that the maximum of the electric-dipole moment results from the influence of the C_1 and possibly C_0 orbits (Fig. 5) on the wave functions:

(i) If the magnetic field is low ($\epsilon > 0.75$), the orbits C_0 and C_1 exist but their modulation amplitudes are so low that they do not influence the excitation spectra. Due to their instability they do not influence the wave functions strongly enough to lead to a large dipole moment, which is inherent to C_0 and C_1 orbits.

(ii) If the magnetic field exceeds the value where maximum dipole deflection is observed ($\epsilon < 0.75$), the C_0 trajectory no longer exists at the ionization energy. The modulation amplitude of C_1, however, is fairly high. Thus individual wave functions should be strongly influenced by the C_1 orbit (this leads to a considerable fraction of strongly deflected atoms, for example, see lower right of Fig. 21). However, the dipole moment of C_1 becomes relatively small for low scaled electric-field strengths (see Fig. 12). This is in agreement with the moderate dipole values which are found experimentally at small scaled electric fields.

(iii) At scaled parameters where the maximum dipole deflection occurs ($\epsilon \approx 0.75$) the C_0 orbit still exists, but exhibits only a moderate modulation amplitude. Therefore an influence of the C_0 orbit on wave functions is quite unprobable. However, the C_1 orbit exhibits for those parameters three successive modulation maxima leading to constantly large modulation amplitudes over a wide parameter range (see Fig. 7). Therefore the observed strongly deflected atoms should correspond to wave functions with dipole moments determined by the influence of the C_1 orbit.

The preceding discussion shows that the large dipole deflection at $\epsilon \approx 0.75$ can be explained by the influence of classical trajectories on wave functions. Since these are usually influenced simultaneously by many trajectories, the dipole moment of a wave function is in most cases much less than that following from the trajectory exhibiting the largest dipole moment. Thus the dipole moment resulting from the deflection measurement has to be smaller than that of the C_0 and C_1 trajectories. A comparison between measured dipole moments and trajectory dipole moments enables us to estimate how strong individual wave functions may be scarred by the high dipole moment trajectories. Figures 20 and 21 show that the maximum scaled electric-dipole moment is 0.70 ± 0.15, which is to be compared to the scaled electric-dipole moment of the C_1 orbit, being 1.0 (see Fig. 5). Thus the measured dipole moment is about two-thirds of the C_1 trajectory dipole moment. This estimate must be seen as a lower limit since in the experiment the measured dipole moment may be smaller than the maximum dipole moment taken during the deflection process [see Eq. (17)]. From the fact that the measured dipole moment reaches two-thirds of the C_1 trajectory dipole moment, it follows that the probability for an electron to be found along the C_1 trajectory is equal or larger than two-thirds, i.e., that individual wave functions must be scarred predominantly by the C_1 orbit.

Finally the experimental results are briefly dicsussed with regard to the numerical calculation which was done in connection with the potential Eq. (8). With increasing magnetic field the plots in Fig. 3 which are discussed in Sec. II B become more and more symmetric and are reduced in size. The contraction of the space which is accessed by trajectories starting at the core reflects the fact that orbits of the C_1 type as well as all others contract more and more as the magnetic field is increased. The average electric-dipole moments obtained from the (gauge-independent) data sets evaluated in Figs. 2 and 3 agree quite well with the dipole moments of the weakly deflected atoms which correspond to the main body of the deflection patterns shown in Figs. 19 and 21. This statement implies that the averaged electric-dipole moment obtained from the numerical analysis exhibits no maximum at $\epsilon \approx 0.8$. The weak deflection results from wave functions which are influenced in the same order of magnitude by many classical orbits; thus the numerical dipole moment averaged over many, including nonrecurring, trajectories should more or less agree with the actual dipole moment of the weakly deflected atoms. However, when interpreting the observed *maximum* dipole moments, one should not worry too much about Fig. 3. Figure 3 tells nothing about the stability of trajectories nor about the actual dipole moment of individual trajectories. Moreover, the averaging of data over many trajectories disregards the scarring phenomenon which is the central point in our semiclassical analysis: A wave function may be influenced predominantly by a few of many classical orbits. Thus the observed maximum dipole moment may exceed the value averaged over all orbits by a large factor. Therefore Fig. 3 only allows one to make the statement that with increasing ϵ, nonionizing trajectories are present which show increasing extension towards the classical ionization saddle point.

VII. CONCLUSION

In this paper experimental proof is presented that in crossed fields Rydberg atoms with extraordinarily large electric-dipole moments exist if the external fields and the excitation energy are properly chosen. For parameters yielding strongly deflected atoms the electric forces and the magnetic forces acting on the electron at the classical ionization saddle point have the same order of magnitude. The occurrence of Rydberg atoms exhibiting large dipole moments is explained semiclassically by the properties of classical orbits having large trajectory dipole moments.

ACKNOWLEDGMENTS

The authors would like to thank E. Werner and P. F. O'Mahony for many valuable discussions.

---

[1] E.A. Solov'ev, Zh. Eksp. Teor. Fiz. **82**, 1762 (1982) [Sov. Phys. JETP **55**, 1017 (1982)].

[2] E.A. Solov'ev, Zh. Eksp Teor. Fiz. **85**, 109 (1983) [Sov. Phys. JETP **58**, 63 (1983)].

[3] P.A. Braun and E.A. Solov'ev, Zh. Eksp. Teor. Fiz. **86**, 68 (1984) [Sov. Phys. JETP **59**, 38 (1984)].

[4] P.A. Braun, J. Phys. B **18**, 4187 (1985).

[5] P. Cacciani, E. Luc-Koenig, J. Pinard, C. Thomas, and S. Liberman, Phys. Rev. Lett. **56**, 1124 (1986).

[6] P. Cacciani, E. Luc-Koenig, J. Pinard, C. Thomas, and S. Liberman, Phys. Rev. Lett. **56**, 1467 (1986).

[7] P. Cacciani, S. Liberman, E. Luc-Koenig, J. Pinard, and C. Thomas, J. Phys. B **21**, 3473 (1988).

[8] P. Cacciani, E. Luc-Koenig, J. Pinard, C. Thomas, and S. Liberman, J. Phys. B **21**, 3499 (1988).

[9] P. Cacciani, S. Liberman, E. Luc-Koenig, J. Pinard, and C. Thomas, J. Phys. B **21**, 3523 (1988).

[10] J. Pinard, in *Atoms in Strong Fields*, edited by C.A. Nicolaides, C.W. Clark, and M.H. Nayfeh (Plenum, New York, 1990).

[11] F. Penent, D. Delande, F. Biraben, and J.C. Gay, Opt. Commun. **49**, 184 (1984).

[12] F. Penent, D. Delande, and J.C. Gay, Phys. Rev. A **37**, 4707 (1988).

[13] E. Korevaar and M.G. Littman, J. Phys. B **16**, L437 (1983).

[14] W.R.S. Garton and F.S. Tomkins, Astrophys. J. **158**, 839 (1969).

[15] A.R. Edmonds, J. Phys. (Paris) Colloq. **31**, C4-71 (1970).

[16] A.F. Starace, J. Phys. B **6**, 585 (1973).

[17] J.C. Castro, M.L. Zimmerman, R.G. Hulet, D. Kleppner, and R.R. Freeman, Phys. Rev. Lett. **45**, 1780 (1980).

[18] J.C. Gay, D. Delande, and F. Biraben, J. Phys. B **13**, L729 (1980).

[19] N.P. Economou, R.R. Freeman, and P.F. Liao, Phys. Rev. A **18**, 2506 (1978).

[20] A. Holle, G. Wiebusch, J. Main, B. Hager, H. Rottke, and K.H. Welge, Phys. Rev. Lett. **56**, 2594 (1986).

[21] J. Main, G. Wiebusch, A. Holle, and K.H. Welge, Phys. Rev. Lett. **57**, 2789 (1986).

[22] G. Wiebusch, J. Main, K. Krüger, H. Rottke, A. Holle, and K.H. Welge, Phys. Rev. Lett. **62**, 2821 (1989).

[23] C. Iu, G.R. Welch, M.M. Kash, L. Hsu, and D. Kleppner, Phys. Rev. Lett. **63**, 1133 (1989)

[24] C. Iu, G.R. Welch, M.M. Kash, D. Kleppner, D. Delande, and J.C. Gay, Phys. Rev. Lett. **66**, 145 (1991).

[25] M.C. Gutzwiller, J. Math. Phys. **28/10**, 1979 (1967).

[26] M.C. Gutzwiller, J. Math. Phys. **10/6**, 1004 (1969).

[27] M.C. Gutzwiller, J. Math. Phys. **11/6**, 1791 (1970).

[28] M.C. Gutzwiller, J. Math. Phys. **12/3**, 343 (1971).

[29] M.C. Gutzwiller, Physica **5D**, 183 (1982).

[30] M. Berry, in *Chaotic Behaviour of Deterministic Systems*, Les Houches Session 36, edited by G. Iooss, R.H.G. Helleman, and R. Stora (North-Holland, Amsterdam, 1983).

[31] W.P. Reinhardt, J. Phys. B **16**, L635 (1983).

[32] D. Wintgen, Phys. Rev. Lett. **58**, 1589 (1987).

[33] D. Wintgen and H. Friedrich, Phys. Rev. A **36**, 131 (1987).

[34] D. Wintgen, Phys. Rev. Lett. **61**, 1803 (1988).

[35] D. Wintgen and A. Hoenig, Phys. Rev. Lett. **63**, 1467 (1989).

[36] W. Schweizer, R. Niemeier, H. Friedrich, G. Wunner, and H. Ruder, Phys. Rev. A **38**, 1724 (1988).

[37] E.J. Heller, Phys. Rev. Lett. **53**, 1515 (1984).

[38] E.B. Bogomolny, Physica **D31**, 169 (1988).

[39] M.L. Du and J.B. Delos, Phys. Rev. A **38**, 1896 (1988).

[40] M.L. Du and J.B. Delos, Phys. Rev. A **38**, 1913 (1988).

[41] C.W. Clark, E. Korevaar, and M.G. Littman, Phys. Rev. Lett. **54**, 320 (1985).

[42] G. Raithel, M. Fauth, and H. Walter, Phys. Rev. A **44**, 1898 (1991).

[43] S.K. Bhattacharya and A.R.P. Rau, Phys. Rev. A **26**, 2315 (1982).

[44] J.C. Gay, L.R. Pendrill, and B. Cagnac, Phys. Lett. **72A**, 315 (1979).

[45] M. Fauth, H. Walther, and E. Werner, Z. Phys. D **7**, 293 (1987).

[46] D. Kleppner, M.G. Littman, and M.L. Zimmerman, in *Rydberg States of Atoms and Molecules*, edited by R.F. Stebbings and F.B. Dunning (Cambridge University Press, Cambridge, England, 1983).

[47] M.L. Zimmerman, M.G. Littman, M.M. Kash, and D. Kleppner, Phys. Rev. A **20**, 2251 (1979).

[48] D. Delande, F. Biraben, and J.C. Gay, in *New Trends in Atomic Physics*, Les Houches Session XXXVIII, edited

by G. Grynberg (North-Holland, Amsterdam, 1984).
[49] L.P. Gor'kov and I.E. Dzyaloshinskii, Zh. Eksp. Teor. Fiz. **53**, 717 (1967) [Sov. Phys. JETP **26**, 449 (1968)].
[50] H. Herold, H. Ruder, and G. Wunner, J. Phys. B **14**, 751 (1981).
[51] B.R. Johnson, J.O. Hirschfelder, and K.H. Yang, Rev. Mod. Phys. **55**, 109 (1983).
[52] R.F. O'Connell, Phys. Lett. **70A**, 389 (1979).
[53] P.F. O'Mahony, Phys. Rev. Lett. **63**, 2653 (1989).
[54] G. Wunner and H. Ruder, Phys. Scr. **36**, 291 (1987).

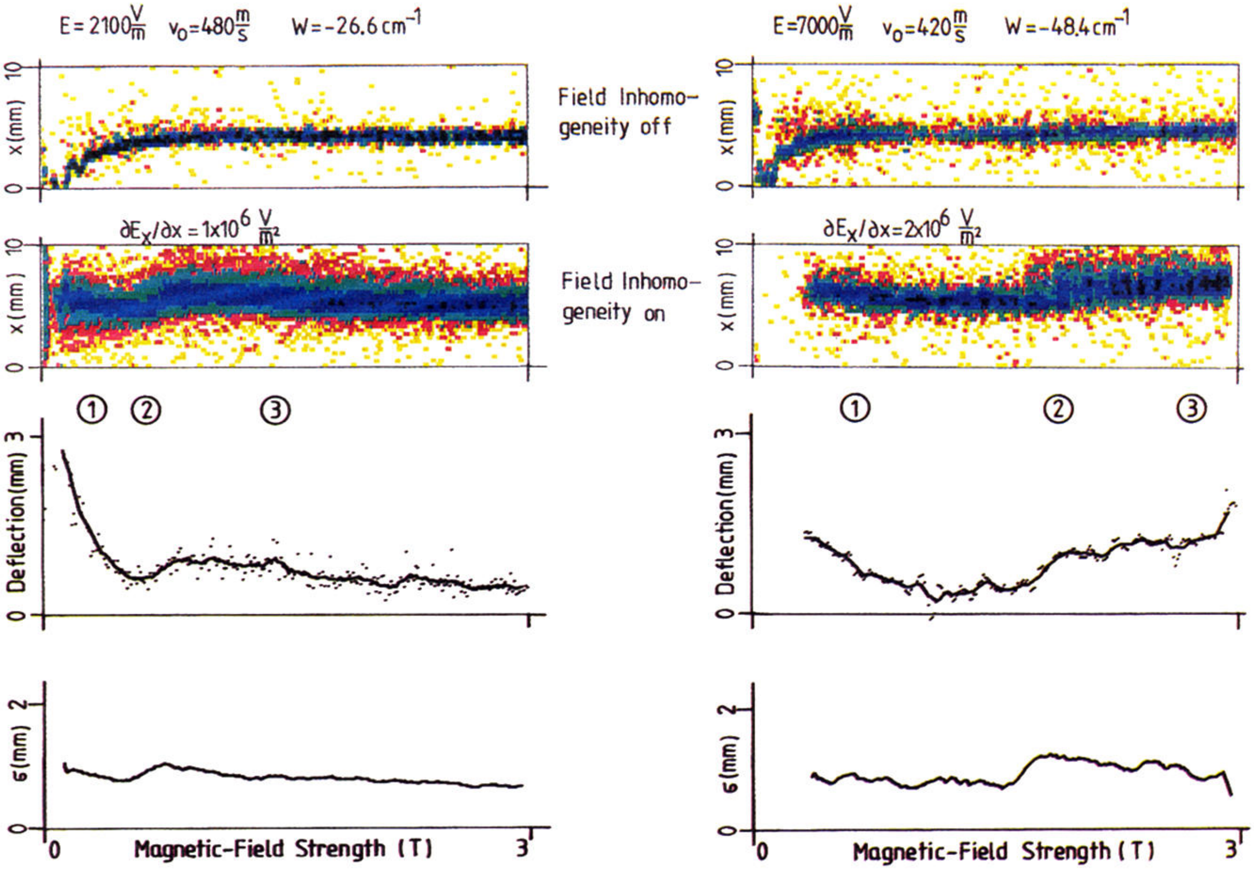

FIG. 18. Dipole deflection at the location of the MCP as a function of the magnetic field for constant electric field and excitation energy close to the ionization energy (two measurements). The number of counts in the pixels increases from yellow to black in a logarithmic scale. The upper images are taken without electric field inhomogeneity, the lower ones with the indicated values of the field inhomogeneity. The deflection as a function of the magnetic field is obtained by subtracting the zero-inhomogeneity atomic-beam position from the average location with applied field inhomogeneity (dots). The solid curve gives the deflection averaged over ten pixels on the B axis. The standard deviation σ is obtained by evaluating the deflection distribution $N(x, B)$ for each magnetic-field value B with respect to x. The interpretation of the increase of the deflection and the standard deviation at certain magnetic-field values is given in the text.

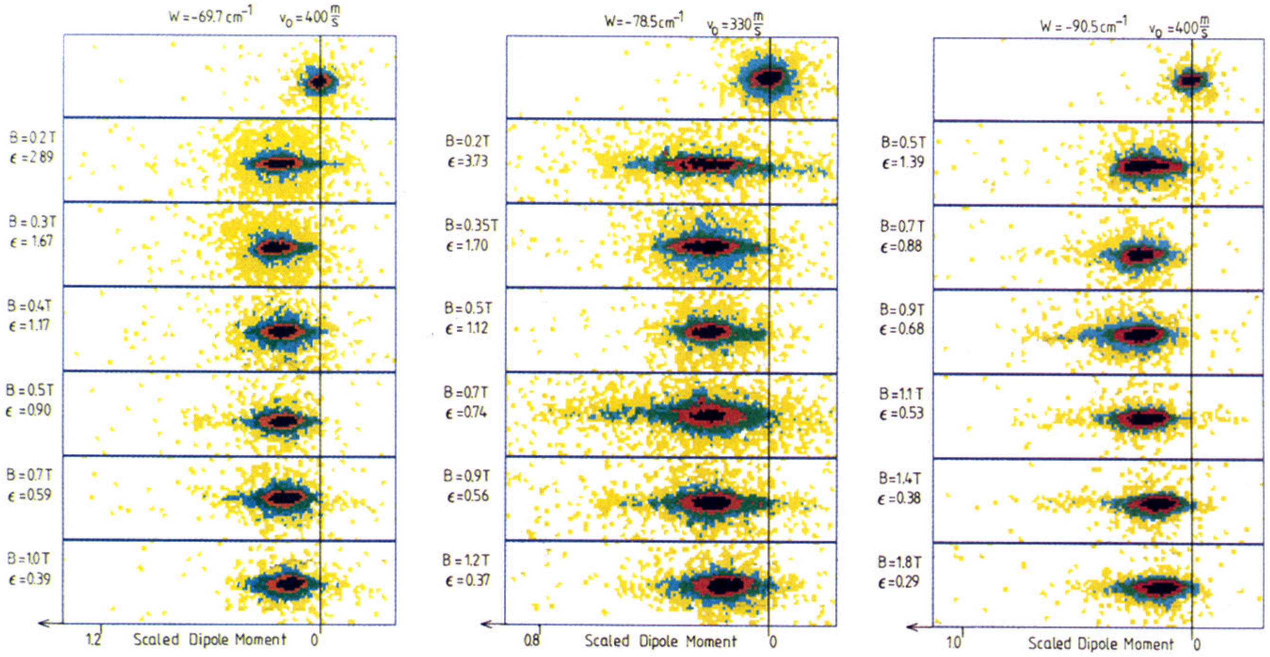

FIG. 19. Three sets of measurements showing the dipole-deflection pattern as a function of the scaled electric field at constant excitation energy, each image taken at the ionization limit. The images show the color-coded two-dimensional deflection patterns on the MCP surface, the color code being normalized to the maximum count number per pixel. The number of detected atoms increases from yellow to black in a logarithmic scale: one color covers a range of 0.477 on the $\log_{10}(n_{(\mathrm{x,y})})$, where $n_{(x,y)}$ is the number of counts in pixel (x, y). The uppermost row of images gives the reference position of the undeflected beam. If a field inhomogeneity is applied, the atoms are deflected in the opposite direction to the electric field, which is directed from left to right. The x axis gives the scaled electric-dipole moment following from the deflection value. It must be emphasized that this value corresponds to the average dipole moment of the atom during the deflection process (see Eq. 17).

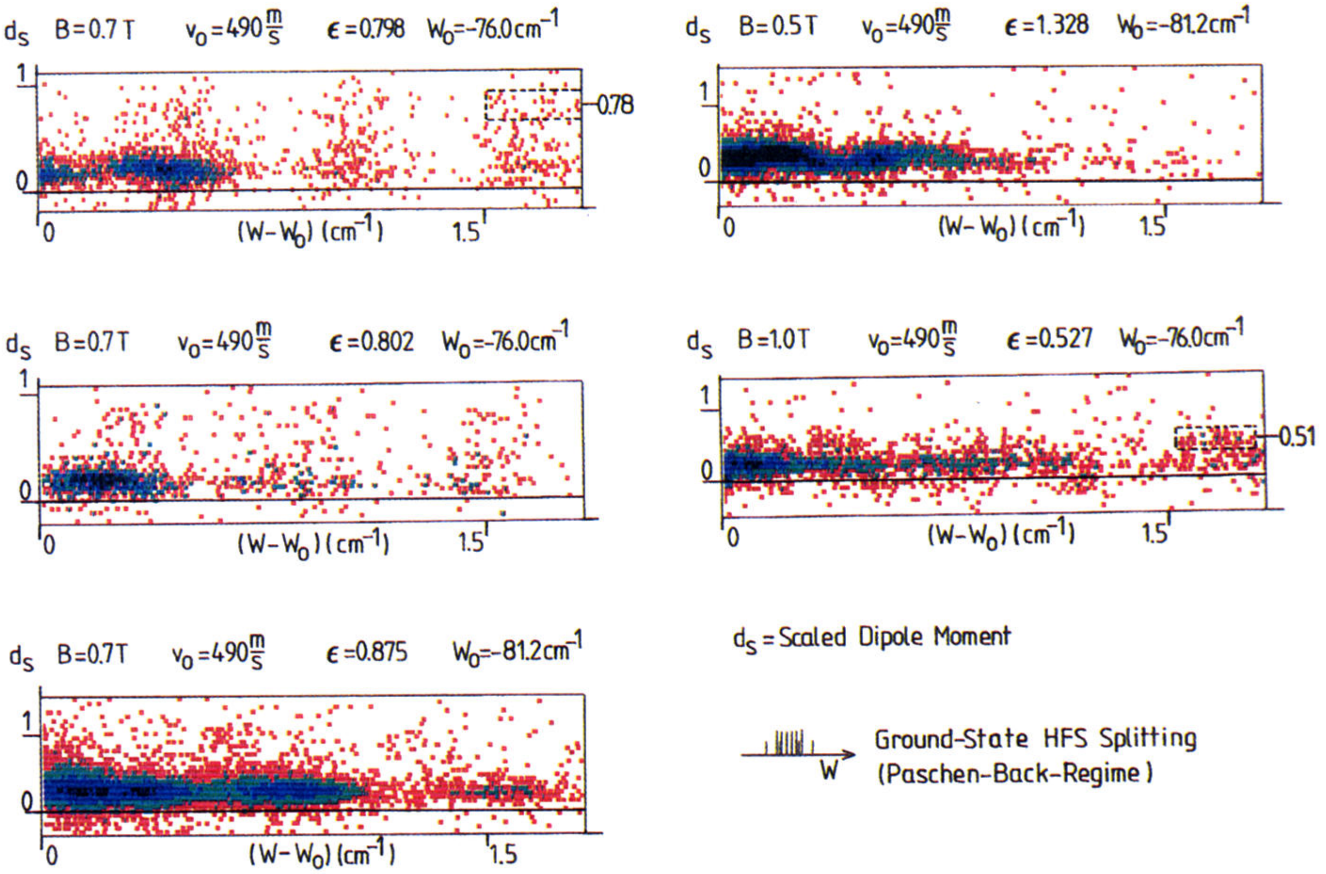

FIG. 21. Scaled average electric-dipole moments as a function of the excitation energy W for different scaled electric fields (color-coded images: the number of detected atoms increases logarithmically from red to black, one color covering a range of 0.477). The deflection spectra are taken very close to the ionization limit. At the large scaled electric field no strongly deflected atoms occur. For $\epsilon = 0.53$ (right column, lower picture) a fairly high fraction of moderately deflected atoms appears. For $\epsilon \approx 0.8$ a few atoms are strongly deflected (left column), the relative number clearly increasing with increasing energy. The width of the bunches of strongly deflected atoms on the energy scale coincides with the width of the ground-state Paschen-Back pattern of the hyperfine structure, being shown in the figure with the same energy scale as the deflection patterns. Some groups of strongly deflected atoms are not correlated with a large counting rate for weakly deflected atoms. This independent behavior ensures that the signals for strongly deflected atoms are not just caused by noise.